

**CONFINEMENT OF NUCLEATION SITES IN NUCLEATE POOL BOILING USING
ATOMIC LAYER DEPOSITION AND CONSTRICTIVE HEATERS**

by

Gregory Raymond Stehle

Bachelor of Science, University of Pittsburgh, 2008

Submitted to the Graduate Faculty of
Swanson School of Engineering in partial fulfillment
of the requirements for the degree of
Doctorate of Philosophy

University of Pittsburgh

2017

UNIVERSITY OF PITTSBURGH
SWANSON SCHOOL OF ENGINEERING

This dissertation was presented

by

Gregory Raymond Stehle

It was presented on

December, 6, 2016

and reviewed by

David Schmidt, PhD., Assistant Professor, Department of Mechanical Engineering and
Material Science, University of Pittsburgh

David Aumiller, PhD., Adjunct Associate Professor, Department of Mechanical Engineering
and Material Science, University of Pittsburgh

Jung-Kun Lee, PhD., Associate Professor, Department of Mechanical Engineering and
Material Science, University of Pittsburgh

Dissertation Director: Mark Kimber, PhD., Assistant Professor, Department of Nuclear
Engineering, Texas A &M University

Copyright © by Gregory Raymond Stehle

2017

CONFINEMENT OF NUCLEATION SITES IN NUCLEATE POOL BOILING USING ATOMIC LAYER DEPOSITION AND CONSTRICTIVE HEATERS

Gregory Raymond Stehle, Ph.D.

University of Pittsburgh, 2017

Boiling heat transfer is a powerful cooling mechanism used in a variety of industries to efficiently dissipate heat by taking advantage of latent heat. Nucleation site interactions have been demonstrated to affect behaviors in the bulk fluid, in the solid substrate and coalescence. Despite extensive studies of multi-site interactions, the conclusions of these studies are not in agreement. Namely, hydrodynamic effects are explained by some studies to promote nucleation while other studies find that, even with thermally isolated heat supplies, the presence of nearby sites diminishes nucleation. The present study identifies superheated fluid as a possible explanation for this variability. Hydrodynamic factors are determined to only promote single site nucleation if there is an appreciable thermal boundary layer present. Even with a thermal boundary layer, the presence of other sites causes competition over the superheated fluid; thus, diminishing the promotive effects of hydrodynamic factors. There have also been studies that have characterized the changing dimensions of the microlayer and the heat transfer that occurs beneath it. However, there is not a complete study of bubble behavior resulting from varying heater areas; specifically heater areas smaller than the microlayer. The present study quantifies the effect of heater diameter on vapor effectiveness and determines the optimal heater diameter. A metric for the coincidence of vapor production and microlayer coverage is proposed. Vapor effectiveness and the coincidence metric are shown to have similar relationships with heater diameter.

TABLE OF CONTENTS

1.0	INTRODUCTION AND MOTIVATION	1
1.1	PRACTICAL USES OF BOILING	1
1.2	METRICS FOR BOILING PERFORMANCE	2
1.3	BUBBLE INTERACTION STUDIES	5
1.3.1	Single-Site Studies.....	5
1.3.2	Multiple-Site Studies	8
1.3.3	Microlayer Studies.....	12
1.4	CONTRIBUTIONS	16
2.0	MATERIALS AND EXPERIMENTAL METHODS.....	19
2.1	BOILING FACILITY DESIGN.....	19
2.1.1	Image Scaling	28
2.2	APPARATUS RECONFIGURATION FOR SMALL HEATER AREAS ..	31
2.3	SURFACE FABRICATION AND CHARACTERIZATION	34
2.3.1	Biphilic Spot Size Study	34
2.3.2	Varying Heater Area Surface Modification	38
2.3.3	Thermal Effect of the TiO₂ Coating.....	40
2.4	EXPERIMENTAL PROCEDURE	41
2.5	IMAGE ANALYSIS	42

2.5.1	Convention for Image Post Processing	42
2.5.2	Determining the Volume of a Bubble Using the Disc-Stacking Method ..	47
2.5.3	Approximating the Volume of a Bubble Using Its Width.....	49
3.0	VAPOR GENERATION OF TEST SURFACES	51
3.1	MULTI-SITE BUBBLE SEQUENCE STUDY.....	52
3.2	SINGLE-SITE BUBBLE SEQUENCE STUDY	61
3.3	SINGLE-SITE BUBBLE GROWTH STUDY	70
4.0	FUTURE WORK	82
5.0	CONCLUSION.....	84
	APPENDIX A	86
	APPENDIX B	89
	APPENDIX C	94
	BIBLIOGRAPHY.....	96

LIST OF TABLES

Table 1 Contributions of The Present Work.....	17
Table 2 Average Roughness of Coated and Uncoated Regions	36
Table 3 Average Contact angle of Coated and Uncoated Regions	37
Table 4 Contributions of Present Study	85

LIST OF FIGURES

Figure 1 Typical Pool Boiling Curve [1]	3
Figure 2 Superheated Pocket Formed By Superheated Liquid Layer Drawn Inward By Bubble Wake Measured by Yabuki and Nakabeppu [8]	7
Figure 3 Measurement of Dry Spot Growth Under a Growing Bubble in Methanol By Jawurek [24]	14
Figure 4 Measurement of Dry Spot Growth Under a Growing Bubble in Water By Jung & Kim 2015 [39]	15
Figure 5 Boiling Facility Diagram	20
Figure 6 Cartoon Depiction of Temperature Distribution within the Heater Rod	21
Figure 7 Comparison of Heat Losses and Total Power	22
Figure 8 Diagram of Ring Boiling	26
Figure 9 Infrared Camera Display Showing Uniform Temperature Distribution. Temperature is shown in °C	27
Figure 10 Image of Hole in Boiling Rig Base Used as Visual Scale	29
Figure 11 Image of Keystock Used as Visual Scale for Single Nucleation Site Studies	30
Figure 12 Diagram of Heater Tip Geometries	32
Figure 13 Diagram of Heater, IR Camera, and Visual Scale	33
Figure 14 Illustration of IR Image of Heater and Scale for Post Processing	33
Figure 15 Photos of Coated Surfaces	35
Figure 16 Image of Indenter Scribe Under Optical Comparator	38

Figure 17 Cartoon of Nucleation Site Indent With and Without Coating	39
Figure 18 Image of Two Indents at 1000x Magnification	40
Figure 19 Contrasting an Unperturbed Bubble with a Perturbed Bubble	43
Figure 20 Illustration of Vertical Coalescence 0.001s Time Step	44
Figure 21 Illustration of Declining Coalescence 0.001s Time Step	45
Figure 22 Illustration of Horizontal Coalescence 0.001s Time Step	45
Figure 23 Illustration of Feeder Nucleation Sites 0.001s Time Step	46
Figure 24 Image of Growing Bubble at $T = 0.1\text{ms}, 1.7\text{ms}, 3.5\text{ms}, 6.9\text{ms}, 10.4\text{ms}, 13.7\text{ms}$	48
Figure 25 Comparison of Equivalent Diameter and Bubble Width During Bubble Growth.....	49
Figure 26 Overestimation of Volume by Spherical Approximation as a Function of Spherical Volume.....	50
Figure 27 Comparison of Average 2-Site Superficial Vapor Effectiveness to Average 1-Site Vapor Effectiveness as a Function of Site Spacing	53
Figure 28 Comparison of Coalescence to Superficial Vapor Effectiveness Ratio from Double Site to the Average Single Site. Double Sites spaced at 3.15mm.	55
Figure 29 Comparison of Average Bubble Velocity and Superficial Vapor Effectiveness for Single, Double and Triple Site Configurations.....	57
Figure 30 Comparison of Average Bubble Diameter and Superficial Vapor Effectiveness for Single, Double and Triple Site Configurations.....	58
Figure 31 Comparison of Average Bubble Reynolds Number and Superficial Vapor Effectiveness for Single, Double and Triple Site Configurations.....	59
Figure 32 Cartoon Illustration of Displacement of Superheated Liquid Pocket Resulting From Nearby Nucleation Site	60
Figure 33 Cartoon Illustration of Three Paths for Heat Transfer Out of Solid.....	62
Figure 34 Graph Showing Increased Heat Flux Required For Onset of Nucleate Boiling With Reduced Heater Diameters	63
Figure 35 Graph Demonstrating Increased Heat Transfer Required for Larger Heaters.....	64
Figure 36 Graph of Bubble Reynolds Number and Vapor Effectiveness.....	65
Figure 37 Comparison of Heater Diameter and Vapor Effectiveness	67

Figure 38 Diagram of Heat Flow Near the Microlayer.....	68
Figure 39 Relationship Between Dimensionless Heater Diameter and Vapor Effectiveness	70
Figure 40 Normalized Growth of Bubble Base Diameter and Empirical Approximation of Dry Spot Diameter With Respect to Time	72
Figure 41 Percent of Microlayer that is Heated and Wetted And Dimensionless Bubble Growth Rate with Respect to Normalized Time for 9.52mm Heater	74
Figure 42 Percent of Microlayer that is Heated and Wetted And Dimensionless Bubble Growth Rate with Respect to Normalized Time for 7.94mm Heater	74
Figure 43 Percent of Microlayer that is Heated and Wetted And Dimensionless Bubble Growth Rate with Respect to Normalized Time for 6.35mm Heater	75
Figure 44 Percent of Microlayer that is Heated and Wetted And Dimensionless Bubble Growth Rate with Respect to Normalized Time for 3.18mm Heater	75
Figure 45 Percent of Microlayer that is Heated and Wetted And Dimensionless Bubble Growth Rate with Respect to Normalized Time for 2.00mm Heater	76
Figure 46 Percent of Microlayer that is Heated and Wetted And Dimensionless Bubble Growth Rate with Respect to Normalized Time for 1.50mm Heater	76
Figure 47 Percent of Microlayer that is Heated and Wetted And Dimensionless Bubble Growth Rate with Respect to Normalized Time for 1.00mm Heater	77
Figure 48 Percent of Microlayer that is Heated and Wetted And Dimensionless Bubble Growth Rate with Respect to Normalized Time for 0.80mm Heater	77
Figure 49 Heater Diameter Compared to Coincidence of Heater Coverage by Microlayer.....	79
Figure 50 Dimensionless Heater Diameter Compared to Coincidence of Heater Coverage by Microlayer.....	79
Figure 51 Heater Diameter Compared to Average Coincidence of Heater Coverage by Microlayer.....	80
Figure 52 Suggested Configurations for Practical Engineered Heater Surfaces	83
Figure 53 Diagram of differential element	86
Figure 54 Contact Angles Surfaces 1 through 4. Left Column Hydrophilic Right Column Hydrophobic	89
Figure 55 Surface 1 Hydrophobic Region Ra 28.21nm.....	90
Figure 56 Surface 2 Hydrophobic Region Ra 72.67nm.....	90

Figure 57 Surface 3 Hydrophobic Region Ra 58.33nm.....	91
Figure 58 Surface 4 Hydrophobic Region Ra 34.46nm.....	91
Figure 59 Surface 1 Hydrophilic Region Ra 23.73nm	92
Figure 60 Surface 2 Hydrophilic Region Ra 31.86nm	92
Figure 61 Surface 3 Hydrophilic Region Ra 29.99nm	93
Figure 62 Surface 4 Hydrophilic Region Ra 33.86nm	93
Figure 63 Comparison of Dimensionless Site Spacing and Departure Frequency for Double Site Configurations.....	95
Figure 64 Comparison of Dimensionless Site Spacing and Superficial Vapor Effectiveness Ratio for Double Site Configurations.....	95

PREFACE

I am grateful for my time spent at the University of Pittsburgh. I've benefitted from a rich education and been a part of a driven and close-knit group of academic professionals within and outside my research group. Deciding to work for Dr. Mark Kimber in his research group was the happiest decision I made as a graduate student. Thank you, Dr. Kimber and each member of the Kimber group. I also want to thank Thorin Tobiassen, Andy Holmes and Charles (Scooter) Hager for sharing their time and invaluable experience with me. Thank you to my family and friends, especially my parents who have supported me unconditionally. Most of all, I want to thank my wife, Becky, for sharing her patience, strength and love.

1.0 INTRODUCTION AND MOTIVATION

Boiling is an effective mode of heat transfer used widely in the power generation industry. There is a long history of boiling studies, but due to its complexity and the vast range of length scales that dictate performance, there is still much that is left misunderstood or even unknown. The following sections discuss the importance of boiling studies and highlight studies that have enhanced understanding. Also, shortcomings are identified and the outline of the research is presented.

1.1 PRACTICAL USES OF BOILING

Boiling is a heat transfer process of great practical interest due to its ability to transfer large amounts of heat with comparatively low temperature rises. It is used extensively for power generation in the steam cycle. More specifically, in nuclear power generation, boiling is seen in boiling water reactors as well as modern pressurized water reactors. In both cases, boiling heat transfer is used to cool the nuclear fuel material. While boiling is very effective for this task, there are limitations to its practicality. At a very high heat flux, the generation of vapor can outpace the ability of the surface to rewet nucleation sites resulting in the formation of a vapor blanket. This blanket acts as an insulator and often causes the heater surface temperature to rise beyond safe temperature limits. This phenomenon is known as critical heat flux, CHF. Similarly,

at low heat fluxes where no boiling occurs, there is a point where natural convection transitions to nucleate boiling. This results in a sharp drop in surface temperature due to a sudden increase in cooling via the phase change process. This is known as the onset of nucleate boiling, ONB. Both ONB and CHF are dependent upon fluid and solid properties, surface configuration, and flow conditions. Engineers rely upon empirically derived correlations to predict these behaviors. However, the few mechanistic predictions that are available for boiling behavior are not sufficiently accurate for practical use. More directly, there are no boiling correlations based on first principles that can predict behavior of a real surface. Better understanding of the mechanisms that influence boiling behavior can lead to enhancement or, ideally, replacement of empirical correlations. Greater accuracy in the prediction of boiling behavior allows power plants to operate more safely and economically.

Applications where boiling is used typically introduce forced convective flow which enhances many, but not all, aspects of boiling performance. Pool boiling occurs in an otherwise quiescent body of water, and experiments of this type are generally simpler and less expensive than flow boiling experiments. However, pool boiling experiments still offer insight into complex boiling phenomena that are not fully understood in either configuration. In the study presented in this thesis, the behavior of saturated water in pool boiling on a horizontal heater surface is examined exclusively.

1.2 METRICS FOR BOILING PERFORMANCE

There are a number of metrics to quantify the complex behavior of boiling. One of the most powerful ways to characterize boiling performance is to generate and analyze a boiling curve.

The boiling curve compares measured excess temperature to heat flux. Excess temperature, T_e , is defined as the bulk fluid temperature subtracted from the surface temperature. In the case of saturated pool boiling, the bulk fluid temperature is the saturation temperature. Heat flux, q'' (units of W/m^2) is defined as the heat input by the area through which the heat is transferred.

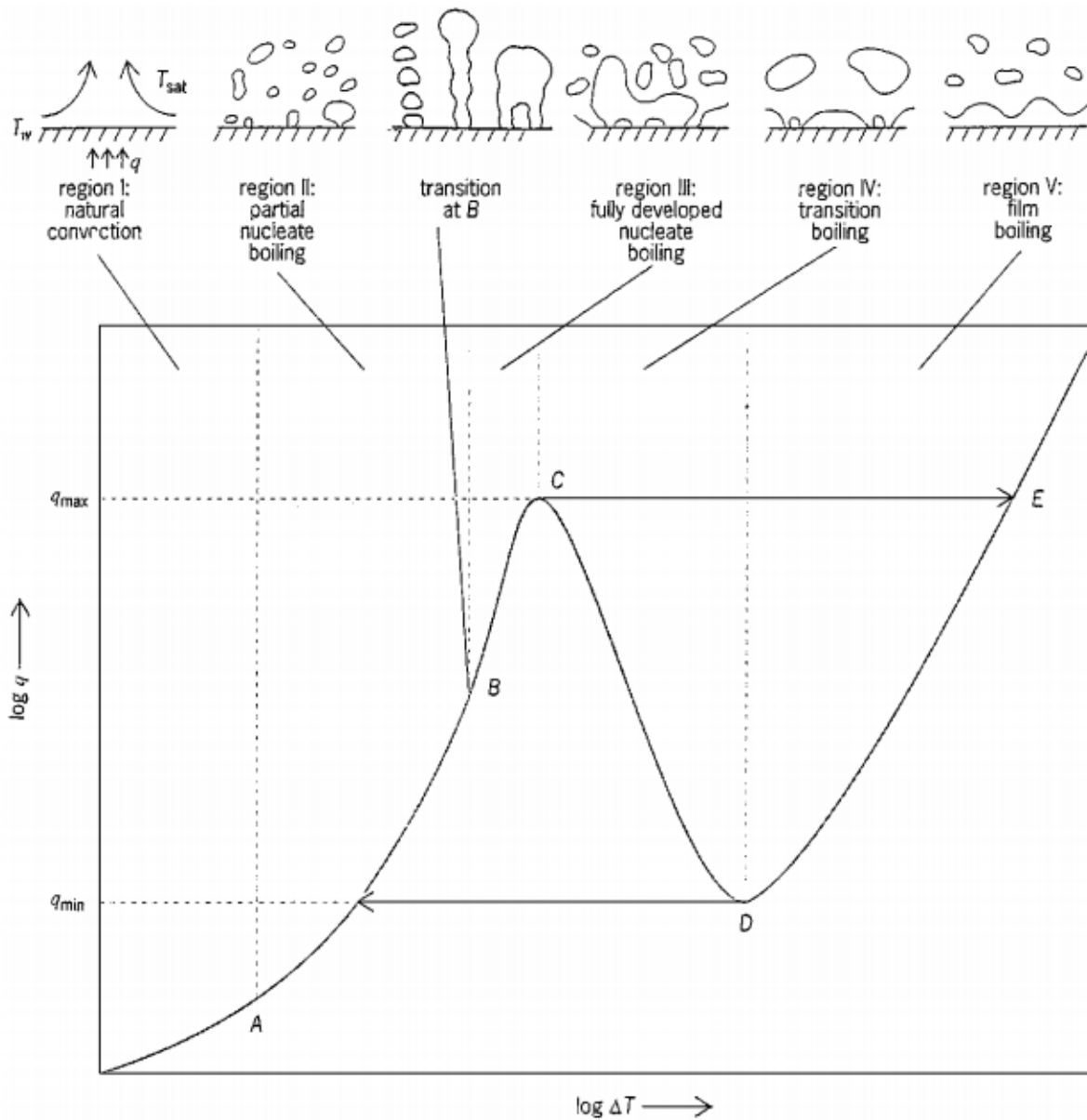


Figure 1 Typical Pool Boiling Curve [1]

A representative boiling curve for pool boiling is shown in Figure 1 and reveals several interesting behaviors as previously mentioned. The first observation is the line leading to point A. This line represents the curve that results from natural convection only, before any heat is transferred via the phase change process. Although not shown in Figure 1, as heat flux is increased, there can be a brief drop in excess temperature that accompanies the onset of nucleate boiling for a heat flux controlled surface. Additionally, the slope of the boiling curve steepens as vapor generation begins at the onset of nucleate boiling. This change in slope is related to the increase in heat transfer coefficient resulting from the additional latent and sensible heat removal from boiling, as well the influence vapor production has on the convective currents providing the cooling. From point A to point C is called the nucleate boiling regime. Point C is known as the critical heat flux and is the point where the nucleate boiling regime ends. For heat flux controlled surfaces, a large jump in temperature (typically hundreds of degrees) occurs after CHF (represented by the line from C to E), and can be disastrous for many applications. Transition and film boiling are two additional boiling curve regimes often explored, but are not discussed here since all of the behavior observed in the current study is well below the critical heat flux and falls into the nucleate boiling regime.

The boiling curve data can be manipulated to quantify the heat transfer coefficient as a function of heat flux. As previously noted, the slope of the boiling curve is related to the heat transfer coefficient. In reality, heat transfer coefficient is equivalent to the slope of a line drawn from the point on the saturated boiling curve to the origin.

Several dimensionless groups are commonly used for the analysis of nucleate boiling. Many of these dimensionless groups are simple adaptations of dimensionless groups used for single phase convection. In each case, the length scale of importance is the bubble diameter, D_b . The

bubble Reynolds number is helpful for exploring what behaviors are influenced by hydrodynamic factors.

The bubble Reynolds number, Re_b , Equation (1) is defined as the ratio of inertia forces to viscous forces. The velocity of interest is the translational velocity of the bubble, V_b . The liquid properties dominate the viscous forces while inertia forces result from vapor motion. Therefore μ_l and ρ_v are employed in the denominator and numerator, respectively.

$$Re_b = \frac{D_b V_b \rho_v}{\mu_l} \quad (1)$$

1.3 BUBBLE INTERACTION STUDIES

Bubble interaction studies have been performed in a variety of configurations. The studies discussed here include single and double sites. While simple, these studies reveal behavior that can be useful for more complex two phase situations.

1.3.1 Single-Site Studies

Single nucleation site studies are among the simplest ways to explore boiling behavior. This type of study has been adopted by some computational fluid dynamics modelers. However, even the single nucleation site can be seen to have large variability in behavior due to fluid or solid chemistry or heater topography. Behavior of single nucleation sites has been explored by several

different groups. Shoji and Takagi [1] explored the behavior of several nucleation site geometries. Conical, re-entrant and cylindrical cavities were made between 50 micron and 100 micron diameters. Conical cavities produced bubbles intermittently and with high superheats while re-entrant and cylindrical cavities generated bubbles rhythmically and with low superheats. This study showed that a single-site can behave very differently depending on the geometry of the cavity.

Siedel et al. [3] analyzed the growth of a bubble on a 180 micron indentation in copper. They proposed a piecewise function relating the volume of the bubble to the duration of growth. Additionally, they suggested that bubble departure frequency strongly depended upon superheat.

Phan et al [4] found that departure diameter increased with increasing wettability which is contrary to the well-known Fritz correlation. They also examined waiting time and found that, as expected, bubble departure diameter and departure frequency are inversely related. They proposed separate bubble growth sequences for hydrophilic and hydrophobic cavities. The growth sequences are different because of the dependency on the presence of a microlayer which is believed to have an influence on bubble heat transfer. In 2010 Phan et al [5] also proposed a theoretical bubble growth model that relates bubble diameter to contact angle. Although no experiments were performed to support the theory, the model utilizes macro and micro contact angles that change as the bubble grows.

Nam et al. [6] tested superhydrophilic copper with a 15 micron diameter cavity. They proposed a correlation that predicts bubble departure diameter based on contact angle. The correlation is suggested for superhydrophilic surfaces and bubbles with spherical caps.

In a study by Yabuki and Nakabeppu [7] and [8] interferometry is used to detect the temperature distribution near a growing bubble. A superheated layer is observed in contact with

the heated surface as is typical for pool boiling. The superheated liquid layer is drawn in below a departed bubble by its wake. A superheated liquid pocket is formed above the nucleation site during the waiting time. Figure 2 shows the formation of this superheated pocket. The present study makes use of this observation to explain behavior in single and multi-site interactions.

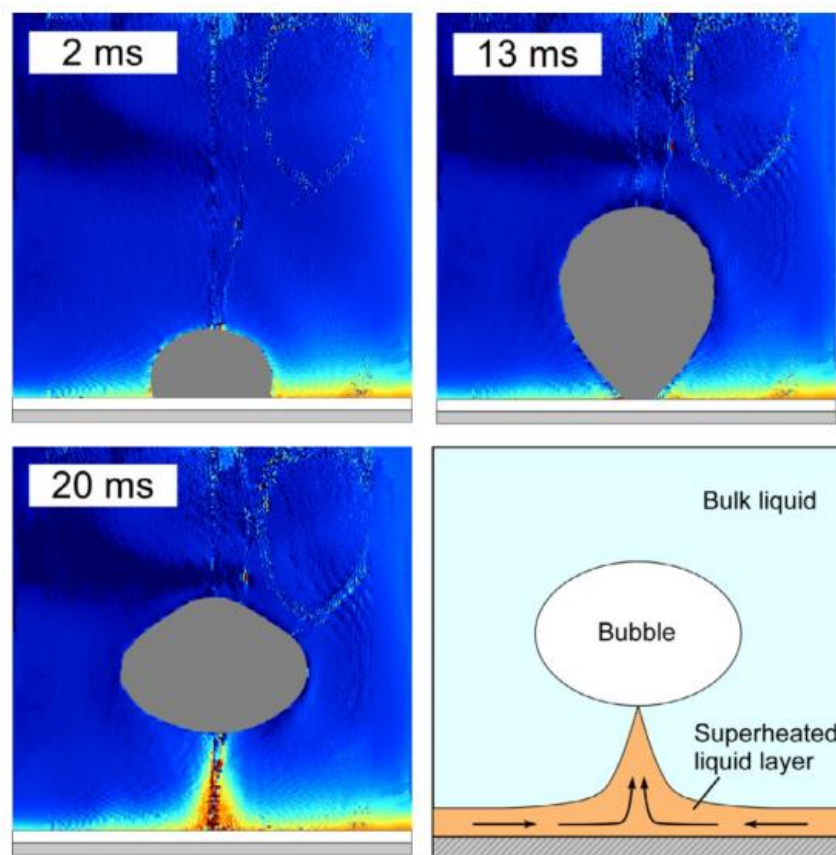


Figure 2 Superheated Pocket Formed By Superheated Liquid Layer Drawn Inward By Bubble Wake Measured by Yabuki and Nakabeppu [8]

None of these studies explored bubble growth on a nucleation site generated by a surface with high contrast wettability patterns. The present study aims to explore the effect of reducing the

hydrophobic area, thereby constraining the number and location of nucleation sites. Although multiple nucleation sites may exist for larger areas of hydrophobicity, sufficiently small areas permit a detailed analysis of bubble departure behavior at the single nucleation site.

These studies explored the behaviors of bubbles growing on a variety of surfaces. However, due to the semi-permanent nature of most of these hydrophilic surfaces, there were no comparisons of identical surfaces with varying wettability. The importance of the cavity geometry was already demonstrated by Shoji and Takagi [1]. Therefore if two surfaces were made, it would be difficult to decouple the effects of the differences in the artificial nucleation sites and, of course the variation in surface topography. One of the goals of the present study is to explore the difference between two nucleation sites that are different in wettability but are otherwise identical.

1.3.2 Multiple-Site Studies

Bubble interaction studies are one of the few possible ways to uncover the physics behind boiling phenomena. Although there have been numerous high-impact studies of bubble interaction, not all findings were in agreement. It is intuitive that two nucleation sites spaced sufficiently far from each other would behave identically with or without the second location, but exactly when and how the two sites become coupled is poorly understood. Typical convention has been to define a dimensionless spacing as S/D_b where S is the distance between nucleation sites and D_b is the bubble diameter. The behavior of neighboring nucleation sites has been broadly classified as inhibited nucleation, promoted nucleation, and no effect. Zhang and Shoji [9] created a dual site study with cylindrical cavities that measured the effects of conduction in the substrate and quantified coalescence behavior with a high speed camera. This study identified

three major influences on bubble departure frequency as hydrodynamic, thermal, and coalescence. Hydrodynamic and coalescence effects were said to promote nucleation while thermal conduction in the substrate was believed to inhibit nucleation. Nucleation sites with dimensionless spacing greater than 3 were found to behave as though they were independent of one another. When S/D_b was between 2 and 3, hydrodynamic effects promoted nucleation. Between 1.5 and 2, the departure frequency was reduced as thermal interference in the substrate played an inhibitive role. And finally, below dimensionless spacing of 1.5, nucleation was again increased due to the promotive effect of coalescence. Chekanov [11] found that regions with S/D_b of less than 3 were inhibited and regions with S/D_b of greater than 3 were promoted. However, Calka and Judd [12] found that inhibited nucleation occurred at S/D_b of less than 1, promoted nucleation occurred at S/D_b between 1 and 3 and no effect was seen with S/D_b of greater than 3. There is clear disagreement regarding the relationship between bubble interaction and dimensionless spacing.

Nimkar et al [13] also explored the relationship between spacing and optimal thermal performance. They found that the best thermal performance was achieved between S/D_b of 1.70 and 2.50. However Golobič and Gjerkeš [14] used individually heated nucleation sites and found that the closer the sites were, the worse the coupled performance. Meanwhile, Bonjour et al [15] explored one, two and three site interactions. They found the thermal performance to be maximized when no coalescence was observed between the nucleation sites. Alternatively, Chen and Chung [16] and [17] found that coalescence contributed to better heat transfer. And still von Hardenberg et al [18] found that nucleation sites became entirely isolated at S/D_b of 1. Siedel et al [3] determined that the layer of water between two coalescing bubbles does not contribute to vapor generation which had been previously believed to evaporate upon coalescence. Hutter et al

[19] found that dimensionless site spacing closer than 1.5 permitted horizontal coalescence. However, site spacing was not seen to have a discernable effect upon departure frequency. Jingliang et al. [20] found that there are important distinctions between coalescences depending on relative bubble size and length of time to departure. These parameters were found to be highly dependent upon the level of heat flux applied.

The study most relevant to the present study was performed by Golobič and Gjerkeš [14] where multiple, individually heated nucleation sites were compared. This and other studies explored departure frequency to evaluate bubble interaction. In [14], the authors analyzed the latent heat required to create the bubbles. Several important observations were made. First, the mere presence of an additional adjacent site caused other sites to reduce their vapor production even though they were being independently heated. Secondly, by increasing the heat load and subsequent vapor production of an individual site, the vapor production of adjacent sites was further reduced and may even have been eliminated despite the fact that its heat supply remained unchanged. Finally, the group of sites as a whole produced less vapor when compared to its input heat as the number of sites was increased.

There is a great deal of variation in these findings. Many of the substrates are standard copper or silicon material with mechanical nucleation sites. The heat fluxes at the surfaces are limited by the onset of nucleate boiling on the surrounding flat surface. Making use of hydrophilic coatings on the surrounding areas delays the onset of nucleate boiling in these regions, allowing behavior to be observed at higher heat fluxes.

The study presented here explores a method for controlling the nucleation of bubbles with a surface enhancement known as atomic layer deposition, ALD. The ALD surface coating method can be used to create thin coatings of TiO_2 and other materials. With the use of a mask, it is

possible to generate patterns in which some areas are coated while others remain uncoated. It is known that surfaces with lower contact angles require greater heat flux to initiate boiling. Therefore, if the substrate contact angle is sufficiently different from that of the coating material, the onset of nucleate boiling, ONB, will be dependent upon the pattern of the coating. It is the expectation that this surface coating method could yield surfaces with high critical heat fluxes, CHF, but do not suffer from poor boiling heat transfer, BHT, in the lower heat flux regimes. Furthermore, repeatable control of bubble nucleation is an important tool in the study of bubble dynamics. The present study demonstrates that, with the use of ALD, it is possible to control which regions of the boiling surface begin to nucleate first. The hybrid nature of the surface affinity to water is a concept recently explored by Betz et al. [21] and [22]. They found that small hydrophobic spots of approximately 40 μm diameter spaced by 50-200 μm within a hydrophilic area yielded better boiling heat transfer and critical heat flux performance than fully hydrophilic or hydrophobic surfaces. The current study aims to use hydrophobic areas to revisit the two-site bubble interaction study.

ALD coatings of suitably small thickness (5-20 nm) are a possible way to control nucleation without appreciable mechanical modification. Controlling nucleation in this manner could be the basis for a new bubble interaction study. The current work aims to demonstrate the practicality of the method as well as to identify some limitations. A single spot of plain stainless steel surrounded by a hydrophilic region serves as the isolated area that experiences nucleation within the heated surface. The spot diameter is varied to explore the effect of nucleation site confinement within the spot. A high speed camera is used to measure bubble departure frequency, diameter, and velocity while applying various heat fluxes. The examination of a

single hydrophobic spot is the first step toward multiple-site studies using this technology, which is discussed in Chapter 4.

1.3.3 Microlayer Studies

The microlayer is a thin film of liquid between a bubble in hemispherical growth and the heated surface. Evaporation of the microlayer is a major contributor to bubble growth. The measurement of microlayer geometry and heat transfer has been the subject of studies ranging back to a conclusion by Moore and Mesler [23] that a microlayer must be present under bubbles they are observing. They had seen in previous studies that a microlayer was present for stagnant bubbles and was measured to be $0.15\mu\text{m}$ in thickness. Their calculations suggested that the microlayer thickness would be in the range of $2\ \mu\text{m}$ which is very reasonable even by modern estimates. However, the shape of the microlayer is subject to change with time. Indeed, a dry spot forms at the microlayer center, and grows until the microlayer is depleted. The outer diameter is the bubble base diameter which also grows and shrinks until the bubble departs. Jawurek [24] characterized the transient microlayer and dry spot geometry of methanol. This study is of particular interest due to the clear representation of the dry spot growth. The astute reader will recognize the near-linear growth of the dry spot to meet the bubble base diameter at approximately 78.5% of growth time (see Figure 3). While the experimenters used organic fluid under subcooled conditions, this trend has been observed in later studies better aligned with the conditions of the present study. A study by Koffman [25] briefly discussed the development of the dry spot but mostly in a qualitative sense. Cooper & Lloyd [26] successfully measured and reported microlayer thickness and dry spot development. Myers et al. [27] identified and measured the transient heat transfer associated with the rewetting of the dry spot. Das et al. [28]

developed a heat transfer prediction method that accounts for the microlayer, macrolayer and dry spot. Golobic et al. [29] measured the time varying heat temperature, heat flux and heat transfer coefficient on a thin titanium foil. While the dry spot did have reduced heat flux, there was still a significant heat transfer coefficient measured at the centerline. In a later multisite study [30] with the same setup, the maximum heat transfer coefficient was again measured at the centerline with the maximum heat flux occurring at the triple contact line. Gao et al. [31] measured the microlayer geometry from below the bubble using a clear heater and interferometric laser measurements. Utaka et al. [32] found that the percent of total vapor generation resulting from microlayer heat transfer increases with increasing surface superheat. The Buongiorno group contributed a great deal to the microlayer heat transfer discussion. Gerardi et al. [33] measured heat transfer and lateral microlayer geometry. Kim et al. [34] measured the triple contact line and microlayer geometry from the underside of a bubble using a clear heater. Kim et al. [35] also measured the wetted area fraction on a multi-site surface and found that increasing heat flux results in monotonic decrease in wetted area fraction. Duan et al. [36] measured microlayer heat transfer, bubble growth, and liquid flow fields using particle image velocimetry. Buongiorno et al. [37] discussed the current methods for multiphase flow experimentation noting several current microlayer measurement technologies.

Jung and Kim [38] and [39] in an experimental tour de force performed a heat transfer measurement beneath a growing bubble while simultaneously measuring microlayer geometry.

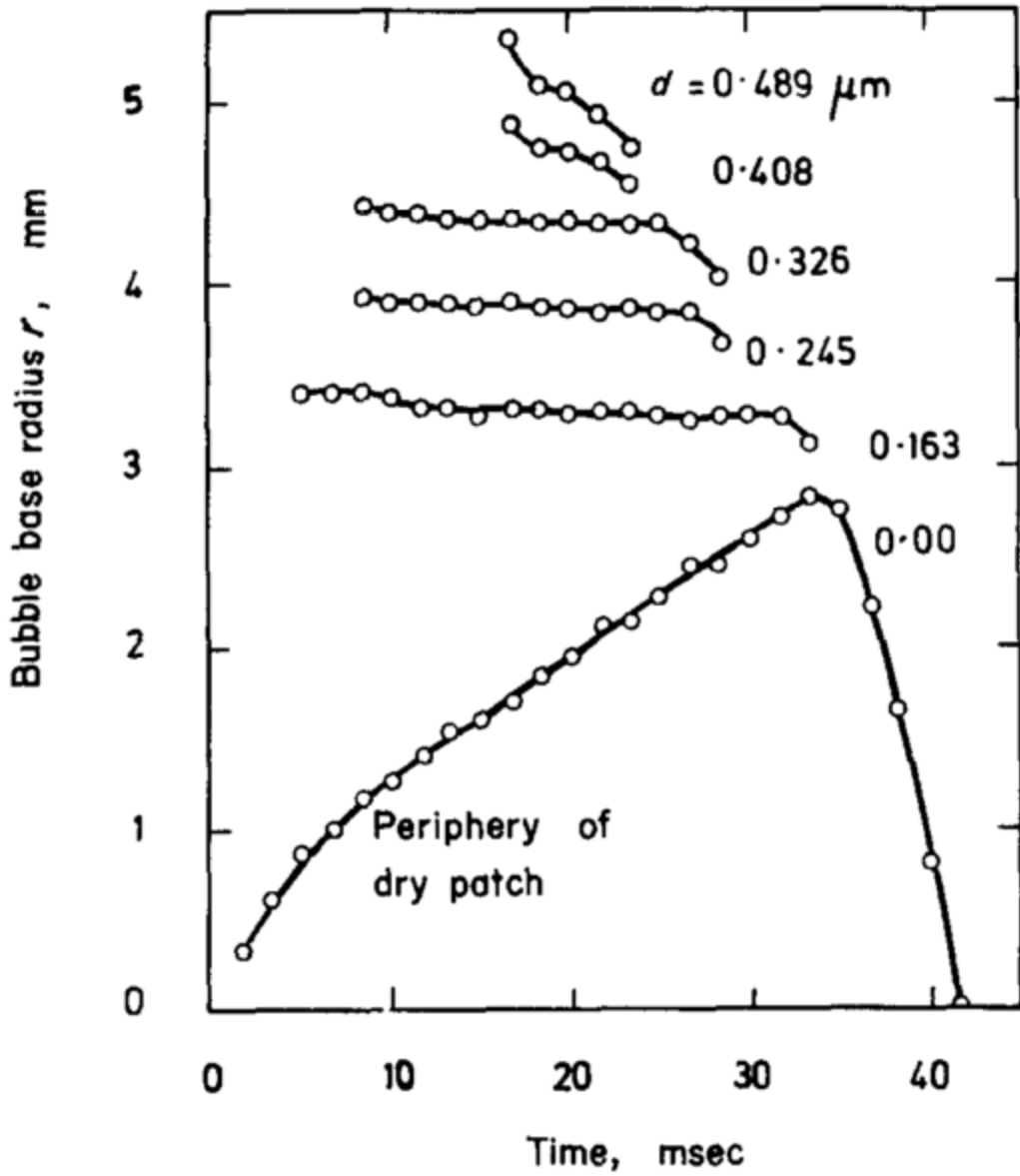


Figure 3 Measurement of Dry Spot Growth Under a Growing Bubble in Methanol By Jawurek [24]

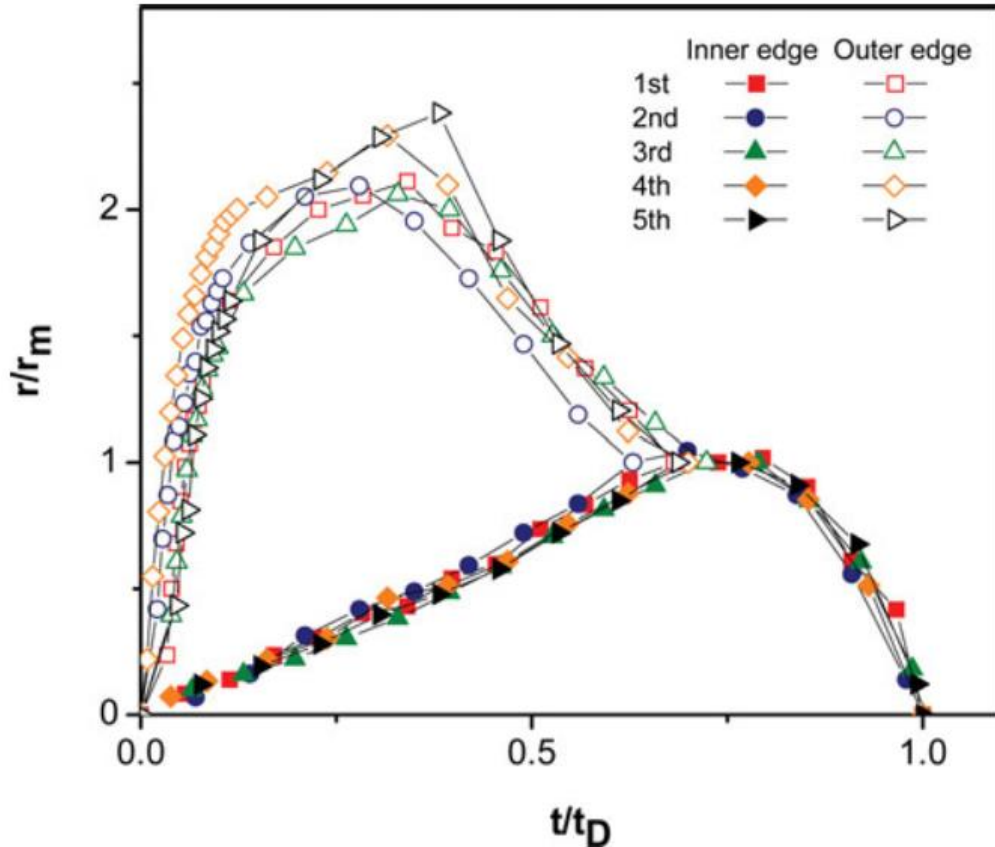


Figure 4 Measurement of Dry Spot Growth Under a Growing Bubble in Water By Jung & Kim 2015 [39]

Both of these behaviors were measured in time and space and are seen in Figure 4. One interesting finding was that the dry spot diameter, again, grew linearly until it met the bubble base diameter between 65-70% of the growth time. This behavior was repeatable across 5 trials in water with a low subcooling of 3°C. Due to its simple implementation, this observation is the basis for the dry spot diameter of the present study.

Few studies have experimented with reducing the heat transfer area beneath a bubble. Golobič and Gjerkeš [14] explored bubbling behavior for multiple-site interactions with varying heater diameters. There was no mention of microlayer in this study, but there was evidence of its effect on heat transfer performance. In a square array, nucleation sites with 1.6mm heater diameters

were compared to the same configuration with 2.2mm heater diameters. In both cases, the nucleation sites produced less vapor when adjacent sites were introduced. However, the 2.2mm heater diameter case was affected less dramatically by the presence of other sites. This result was counter-intuitive as larger heater diameters would seem to be more susceptible by wake effects of adjacent bubbles. The study did not explore the change in vapor production caused by reducing the heater diameter. However, the results suggested that changes in the heated area influence the behavior of site-to-site interaction.

1.4 CONTRIBUTIONS

The present work aims to make contributions in both the single-site and multiple-site areas of bubble interaction studies in nucleate boiling. Each study employs either ALD surfaces or precision heater application to control nucleation on boiling surfaces. Table 1 outlines the contributions made by the present work.

The multisite study first proves that high contrast regions of wettability can control bubble nucleation. It then reframes the discussion of multisite behavior in terms of vapor effectiveness which helps to determine which factors contribute or detract from bubbling. Specifically, the role of hydrodynamics is suggested to be promotive by some studies and inhibitive by others. The present multisite study demonstrates that while promotive for single-site studies, the presence of adjacent sites diminishes the promotive effects of hydrodynamics. The constricted heater single-site study is introduced and helps contribute to the multi-site discussion by observing the same factors in the absence of a thermal boundary layer. As the present study does not have a method for measuring dry spot diameter, observations from two previous studies by Jawurek 1969 [24]

and Jung & Kim 2015 [39] are used to help approximate this behavior. Knowledge of the dry spot growth is important for estimating the coverage of the heated surface by the microlayer. This coverage is demonstrated to be an important contributor to vapor effectiveness. The coverage by bulk fluid or the dry spot is shown to reduce vapor effectiveness. By reducing the size of the heated area, trends of bubble behavior and microlayer performance area evaluated. As the heated area approaches zero, the behavior of a bubble heated through the dry spot can be observed. The study compares the effect of reducing waste heat to the bulk fluid and the effect of heaters too small to effectively heat a wetted area beneath a bubble. A new technique for evaluating the microlayer coverage of the microlayer is presented and shown to be a strong indicator for vapor effectiveness.

Table 1 Contributions of The Present Work

<ul style="list-style-type: none"> • Address inconsistencies in literature regarding the hydrodynamic and thermal effects of site-to-site interactions; namely, that superheated liquid energy is the object of competition between adjacent sites rather than solid conductive energy. Show that hydrodynamic effects enable isolated sites to utilize this energy but limit the ability of multiple sites to do so by unfavorably displacing a superheated pocket of liquid. Show that in the absence of a thermal boundary layer, the influence of hydrodynamic factors is diminished or eliminated.
<ul style="list-style-type: none"> • Employ observations made by Jawurek 1969 [18] and Jung & Kim 2015 [19] to approximate dry spot diameter growth as linear until coincident with bubble base diameter near 0.75 of the growth time.
<ul style="list-style-type: none"> • Demonstrate that microlayer coverage of heated surface is a key factor for effective vapor generation. Dry spot coverage or bulk fluid coverage of the heater are counterproductive to vapor generation.
<ul style="list-style-type: none"> • Develop a metric that evaluates microlayer coverage of the heated area and compares to coincident bubble growth rates. Demonstrate that this metric is a strong indicator of vapor effectiveness.

The remaining chapters of the dissertation include Materials and Experimental Methods, Vapor Generation of Test Surfaces, and Future Work. The devices used in the measure of boiling performance are described. Methods for the experiment and subsequent post processing are also provided. The results of the boiling study are then presented. These include visual observations and data recorded by instruments, as well as generalizations applying to the behaviors. Finally, future studies are proposed and the work is summarized.

2.0 MATERIALS AND EXPERIMENTAL METHODS

The present work involves the use of a boiling apparatus, the fabrication of specialized surfaces to compare boiling performance, and the use of high speed and infrared cameras. Due to the varying demands of the experimental objectives, there are two setups used for the present study. One uses thermocouples to approximate heat flux and the other uses non-contact infrared imaging. Both use a similar high speed camera arrangement. This section outlines the configuration of each of these parts as well as the manner in which they are used in the experiments.

2.1 BOILING FACILITY DESIGN

The pool boiling facility used in this study is illustrated in Figure 5 and is designed to have the following three key features: quickly interchangeable surfaces, conduction-based heat flux measurement and automated boiling experiments. The facility uses a 304 stainless steel heater core, #1, with four inlaid cartridge heaters, #2, to supply a measured and controlled heat input to the thin, stainless steel boiling surface, #6, located at the bottom of the pool. Auxiliary heaters, #11, and reflux condensers, #10, ensure constant temperature and fluid level during experiments.

Bulk fluid temperature is monitored by a thermocouple, #4, positioned in the bulk fluid approximately 120 mm above the boiling surface. To ensure minimal loss of mass, two allihn

reflux condensers, #10, are mounted on the top of the apparatus. Expanding vapor condenses and returns to the pool.

A central inner chamber is used to ensure momentum and thermal isolation. Four glass walls seal the inner chamber from the outer jacket to eliminate convective currents from the auxiliary heater. Heat transfer out of the inner chamber is significantly diminished due to the surrounding saturated water jacket. Finally, the reflux condensers, #10, are positioned above the inner chamber. Water always spills over from the inner chamber to the outer chamber to ensure a consistent water level in the inner chamber. If ever purity in the jacket were to become a concern, only condensed vapor refills the inner chamber.

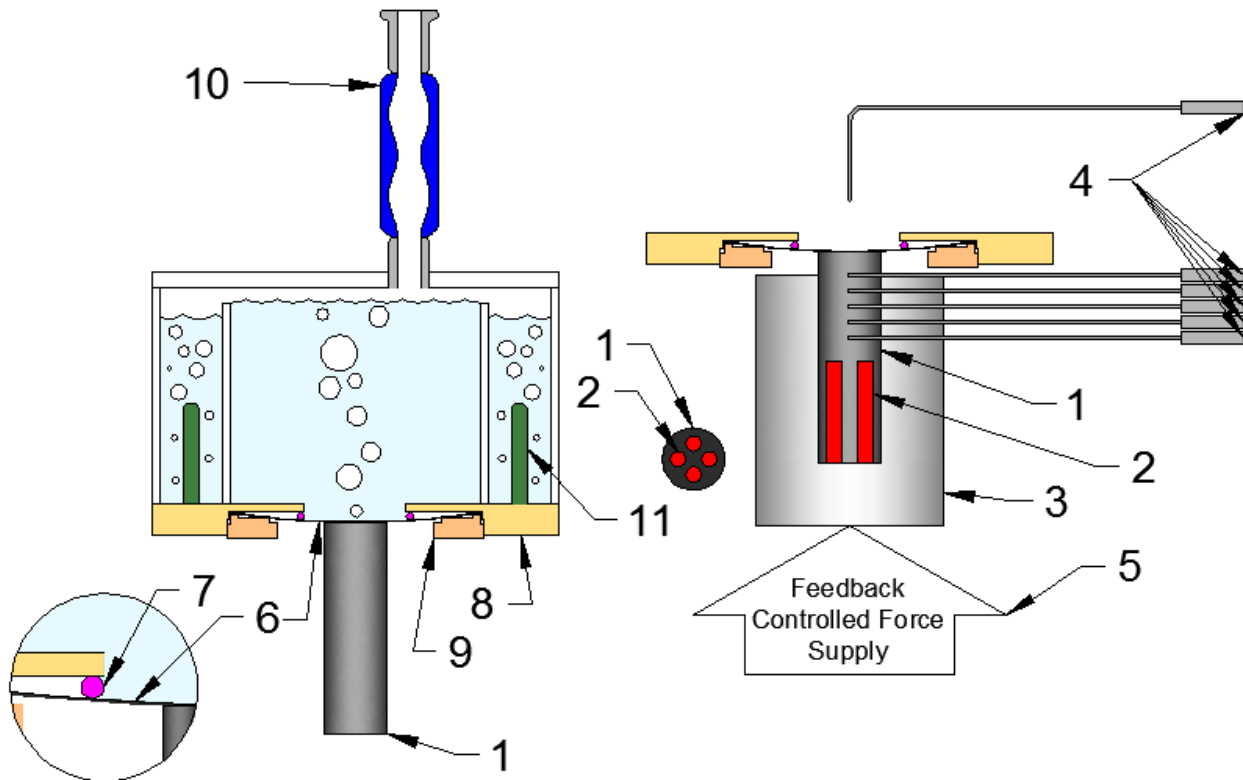


Figure 5 Boiling Facility Diagram

Figure 5 shows five thermocouples, #4, spaced at 6.35 mm intervals along the axis of the 25.4 mm diameter heater core, #1. These are used to measure steady state heat input to the surface. Figure 6 illustrates the temperature distribution within the heater rod. The rod is separated into three regions that are used for different calculation purposes.

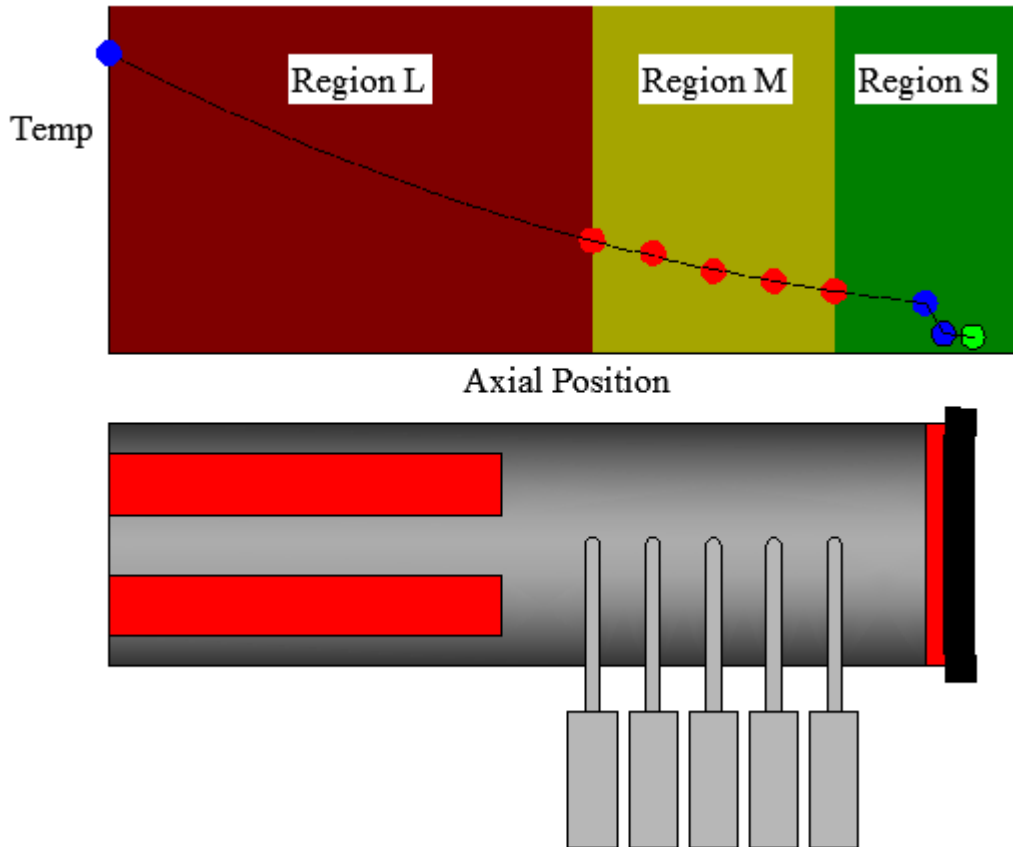


Figure 6 Cartoon Depiction of Temperature Distribution within the Heater Rod

The measurement region is 25.4mm long shown in yellow with the label: Region M. Region M is populated with five thermocouples and is used to determine the parameters that fit temperature as a function of position. Boundary conditions and other parameters are determined in this region. The adjacent regions use the fit that was determined within Region M. Region S is

shown in green and represents the region where surface conditions such as heat flux are calculated. The boundary conditions from Region M help determine the temperature and heat flux at the heater rod end. Finally, region L is where losses are approximated. Losses are assumed to be the difference in heat flux at the two ends of the heater rod. This simplification ignores the effect of internal heat generation along the length of the cartridge heaters. However, the highest temperature should occur at the same point regardless of this consideration. Therefore, the approximation for losses should be reasonable for the purposes of discussion. Figure 7 shows the total power, surface power and heat losses of each data point taken in these experiments. Losses appear to be strongly dependent upon total power input which is in line with expectations. Note that total power is equal to the sum of the surface power and the power lost to the environment.

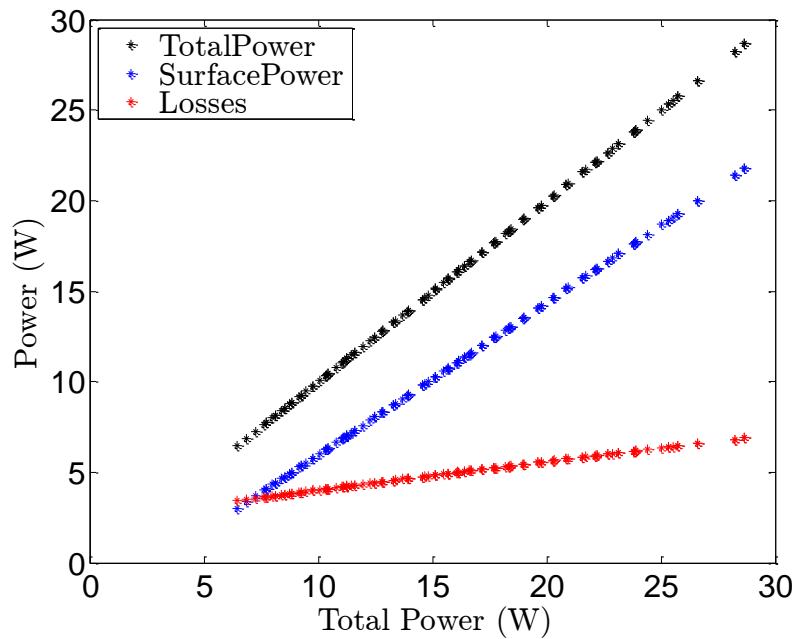


Figure 7 Comparison of Heat Losses and Total Power

As temperature varies by greater than 150 °C along the axis of the rod, variations in thermal conductivity are considered. The model presented by Graves et al [40] is provided in Equation (2), and estimates the thermal conductivity of stainless steel as a second order polynomial function for temperatures between 60°C and 700 °C. In this expression, T is required to have units of Kelvin with the resulting thermal conductivity, k , given in W/m-K

$$k = 7.9318 + 0.023051 \cdot T - 6.4166 \times 10^{-6} \cdot T^2 \quad (2)$$

During experiments, the temperature measurements within the stainless steel will be bounded between 100°C and 300 °C. Fourier's law of heat conduction is employed with the assumption of isotropic material composition in Equation (3). The term dT/dx represents the thermal gradient through the solid.

$$q'' = -k(T) \frac{dT}{dx} \quad (3)$$

The expression for temperature-dependent thermal conductivity is substituted into Equation (4).

$$q'' = \left(-7.9318 - 0.023051T + 6.4166 \times 10^{-6} T^2 \right) \frac{dT}{dx} \quad (4)$$

Knowing the temperature and thermal gradient at any point in the heater rod is sufficient for calculating heat flux. However, due to imperfect insulation, the rod loses some heat to the environment before it reaches the boiling fluid. Therefore, heat flux is not constant along the rod's length. It is assumed that the losses from the rod behave similarly to heat lost in a pin fin. A uniform heat transfer coefficient, h , at ambient temperature, T_∞ , cools the pin's surface. h is approximated empirically to be 4.74 W/m²-K. Therefore, no credit is explicitly given to the

ceramic jacket insulator, #3, depicted in Figure 5. The approximation of h is discussed later in the least squares approximation of temperatures.

Such a configuration is well-approximated by the fin equation for variable thermal conductivity and constant circular cross section as shown in Equation (5).

$$\frac{d^2T}{dx^2} + \frac{1}{k(T)} \frac{dk}{dT} \left(\frac{dT}{dx} \right)^2 - \frac{4h}{k(T)D} (T - T_\infty) = 0 \quad (5)$$

Equation (5) is a form of the fin equation adapted for constant circular cross section and variable thermal conductivity. The derivation for Equation (5) can be found in Appendix A. Equation (5) is a second-order nonlinear ordinary differential equation that describes temperature as a function of position.

The use of a pin fin equation requires the assumption that temperature variations in the transverse direction are small. The Biot number, Bi , is the ratio of the thermal resistance of the solid in the transverse direction to the thermal resistance from the convection at the solid's boundary. Fin conditions with small Biot numbers are well approximated by 1-D fin equations because there are small temperature changes along the width of the fin. The Biot number for a pin fin is expressed in Equation (6) where D is the diameter of the fin and k is the conductivity of the pin material.

$$Bi = \frac{hD}{k} \quad (6)$$

The maximum value of Biot number that was calculated in any experiment was 0.0077 which is considered to be much less than 1. Therefore the use of the 1-D fin equation is considered to be suitable for this analysis.

The solution of Equation (5) requires initial temperature and derivative conditions. These initial conditions are optimized with a least squares curve fitting tool. The heat transfer coefficient, h , cooling the surface of the rod is not known. For each experiment, h is assumed to be constant. Therefore, h is guessed between $0 \text{ W/m}^2\text{-K}$ and $20 \text{ W/m}^2\text{-K}$ with a simple trial and error method. Residual errors for each of the five thermocouple measurements are measured and their absolute values are summed. All of the residual errors are summed for every experimental data point. This process is repeated until the h with the lowest total temperature residual is found. As mentioned previously, the h value that minimizes the error and is used for all calculations is $4.74 \text{ W/m}^2\text{-K}$. With the initial conditions and h known, temperature and heat flux within the rod is easily calculated.

A relationship between contact resistance and interface temperature is generated. The contact area is coated with $0.1500\text{g} \pm 0.0005\text{g}$ of Omegatherm 201 paste. This quantity is chosen because the paste does not run, but coats the entire contact area. The mass of the paste is checked by measuring the mass of an aluminum applicator with a dab of paste. The mass of the applicator is measured again after the application of the paste. The difference in mass is the amount of paste applied to the interface. It is well known that contact resistance between two surfaces is highly dependent on the interface pressure. For this reason, the pressure of the heater core touching the boiling surface is constantly monitored and controlled. As heater power is increased, the temperature of the core increases, causing thermal expansion. Automatic adjustment of the force prevents thermal expansion from increasing pressure. In its un-deformed state, the boiling surface is flat. If the heater core is pressed against the un-deformed boiling surface, the surface will deform and become convex. The cylindrical heater touching the concave side of the surface results in line contact along the circumference of the circular cross section. The result would be

low thermal contact resistance along this line and relatively high thermal contact resistance within the circle. Heat transfers more easily through the contact circle resulting in boiling in the shape of a ring. See Figure 8 below for a graphical illustration of ring boiling. In order to avoid ring boiling, the boiling surface is pre-flexed using a Viton o-ring that also seals the assembly. A large threaded screw presses the outer edge of the surface to force the surface into a concave shape.

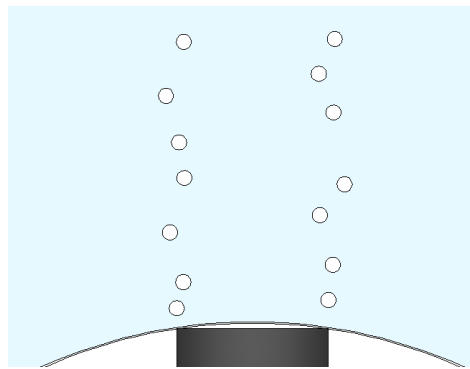


Figure 8 Diagram of Ring Boiling

If the heater core is pressed with a sufficient level of force, the surface will flatten and uniform contact between the heater core and surface will be achieved. To confirm this assumption, a surface is painted flat black and observed with an infrared camera. No water is in the pool and no thermal interface material is used between the heater core and the boiling surface. A small amount of heat is applied to the heater core and the temperature of the surface is recorded. With low forces, the hottest point occurs in the center of the heater core. Higher forces cause the temperature to rise near the circumference. At an intermediate force, the temperature

along the heated surface is uniform. This force was determined to be eight pounds including the weight of the heater assembly. Figure 9 shows the experimental thermal image and the temperature profile along the surface, where the temperature is uniform within 0.1°C within the circular area. Similar results are found to be within a reasonable force range (8 ± 0.25 lb). It is important to note that as the heater core increases in temperature, thermal expansion can cause this force to increase. This apparatus employs a feedback control system to monitor and adjust the force against the surface. An arduino board reads a voltage output from the load cell monitoring the force. When the force needs to be adjusted, the arduino board sends a command to a stepper motor which drives a vertical stage. The movement of the vertical stage changes the load applied to the surface closing the feedback control loop.

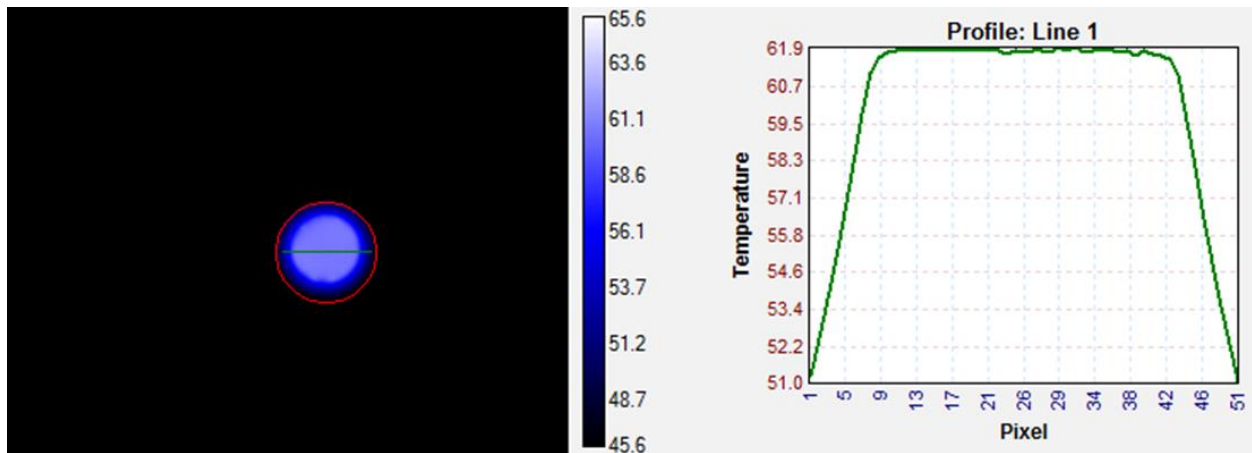


Figure 9 Infrared Camera Display Showing Uniform Temperature Distribution.
Temperature is shown in $^{\circ}\text{C}$

2.1.1 Image Scaling

High speed imaging is performed with a Phantom 7280 high speed camera. Speeds of 100, 1000, and 10000 frames per second are used depending on the needs of the study. The camera is positioned in a consistent manner with respect to the boiling apparatus. In order to view the bubble contact region in the recess of the baseplate, the camera must be directed slightly downward from horizontal. An angle of -16.5° from horizontal is set and measured for each trial. Illumination is provided by a front-lit halogen lamp.

Images are digitized and are delimited by the number of pixels. A scale must be used to know the distance spanned by one pixel and therefore the size of the objects represented by pixels. In the multi-site study, bubbles are free to grow anywhere within a specified area and therefore the high speed camera must cover this specified area. For this reason, the entire surface was captured within the image to ensure full coverage. As such, the opening in the base of the boiling rig is known to be 41.275mm in diameter and is used as a reference for determining the scale of the image. Figure 10 shows a photo of the scale.



Figure 10 Image of Hole in Boiling Rig Base Used as Visual Scale

In the restricted heater diameter study, there is a mechanical indent that serves as a nucleation site. Therefore, the surface generates bubbles much more predictably and permits further zooming in to achieve a better view of the bubble. However, by zooming in on the nucleation site, the reference geometry is no longer in view. Therefore, a visual scale is inserted into the view. A length of 6.35mm square stainless steel keystone is placed directly on top of the nucleation site. Kapton tape is wrapped around the waist of the keystone in two places to prevent scratching of the surface. This piece of keystone serves as a visual scale for determining the size of bubbles being studied. Figure 11 shows a photo of the visual scale.

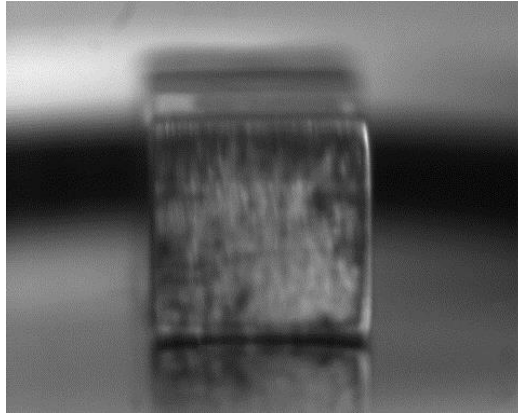


Figure 11 Image of Keystock Used as Visual Scale for Single Nucleation Site Studies

There are several limitations of the boiling apparatus that must be stated. The apparatus in the presented configuration is not suited for high heat flux or CHF measurements. Violent splashing of the inner chamber drives water out and causes unstable water levels. For high heat flux measurements, splash guards and other additions need to be added to maintain a constant water level. Another restriction to high heat flux measurements is the stainless steel heater core. While the lower conductivity of steel increases the temperature gradient, enhancing accuracy, it drives temperatures too high for the instrumentation. The apparatus is set to shut down when thermocouples exceed 300 °C. Aluminum or copper heater cores are suitable to these higher heat fluxes, but their higher conductivity reduces the thermal gradient, sacrificing accuracy. Due to the size of these heater cores, long time constants restrict the ability to perform transient measurements.

As each trial typically lasts multiple days and lab technicians are not available, safety devices and coding are used to protect personnel, the building and the experimental apparatus. The most important barrier to risk is the circuit breaker through which power is supplied. If ever the boiling water were to come into contact with a power supply, the circuit will trip due to the

closed circuit condition. The ability of the circuit breaker to function during a short circuit condition has been verified. A second barrier is the coding used in the matlab program. Temperature is continually monitored and recorded. If temperature readings exceed a specified limit, the matlab program removes power to the heaters. Loss of coolant accidents and critical heat flux are two examples of conditions that will result in a high temperature trip. High temperature conditions have been demonstrated to successfully trip the program. If a loss of coolant occurs but does not cause a high temperature trip, two float switches are used to cut the control signal to the heater power supply, SCR. Loss of coolant in the outer jacket is the condition that would result in the activation of this safety mechanism. This condition has been shown to successfully turn off heater power.

2.2 APPARATUS RECONFIGURATION FOR SMALL HEATER AREAS

The facility is also capable of interchanging heaters to facilitate boiling studies with more precise control of heat application. A variety of heater tips are used to transfer heat through the boiling surface and into the fluid. They range in size from over 9mm in diameter to 0.8mm in diameter. Figure 12 shows the heater tip geometries.

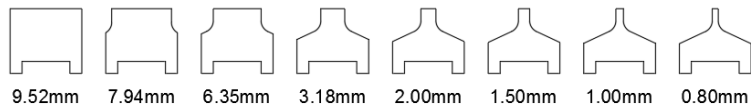


Figure 12 Diagram of Heater Tip Geometries

Figure 13 shows the tip, #1, fitted onto the end of a stainless rod, #2, with a smaller, 80W heater, #3, embedded into the base. This rod is embedded into an alumina ceramic block, #4. This assembly is adapted such that it directly replaces the old heater and insulator assembly. It is also encased in a thin, internally reflective cylinder, #5, to reduce convective losses. Due to the size of the heater, thermocouples are abandoned in favor of non-contact temperature measurement. Each heater tip is painted flat black with paint (Krylon 1602) of known emissivity, 0.95 [41], and a window is cut into the insulating cylinder to obtain an unobstructed view of the heater tip. The temperature distribution is measured with a FLIR SC5000 infrared camera, #6. The calculation of thermal gradient is necessary for determining heat flux. Therefore an accurate spatial reference is required to determine the dimensions in the image. A visual scale, #7 is laser cut from flat shim stock and a grid of lines is laser-etched into the surface.

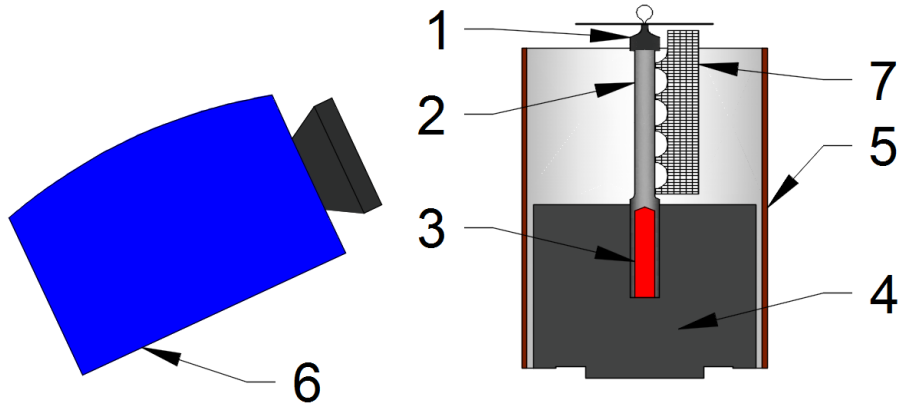


Figure 13 Diagram of Heater, IR Camera, and Visual Scale

Figure 14 shows an IR image of the heater and the underside of the surface. The green vertical “Line 1” is the line over which measurements are taken and the red vertical “Line 2” measures the scale for length measurement. The surface is reflective and it is therefore difficult to see exactly where the end of the heater is. However, the contact point occurs at the location where the temperature gradient reverses.

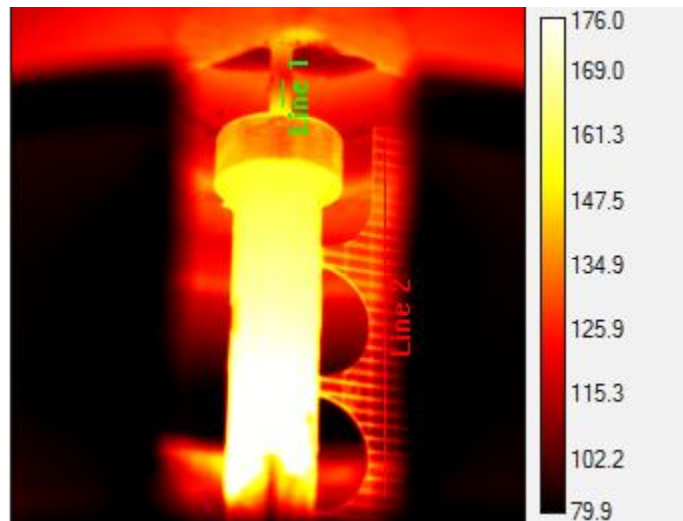


Figure 14 Illustration of IR Image of Heater and Scale for Post Processing

Heat flux is calculated in a similar fashion to the previous configuration, but losses are considered to be negligible due to the short length and proximity of the measurement area to the surface.

2.3 SURFACE FABRICATION AND CHARACTERIZATION

2.3.1 Biphilic Spot Size Study

For the experiments performed, only one substrate is used. The disc is 101.6 mm in diameter and 0.254 mm thick 304 stainless steel material. The surface finish is attained by a progressive sanding to a final 1200 grit roughness. Passivation in 20% nitric acid is performed on the surface after sanding and before coating. This step is taken to help ensure consistent substrate chemistry which may affect wettability as well as the coating process.

Surface coating is performed using the ALD process. A Cambridge Nanotech Savannah S100 is used to apply 15 nm of titanium oxide to the surface. Titanium oxide is known to be highly wettable. Therefore, a contrast in wettability exists between the coated and uncoated portions of the hydrophobic stainless steel substrate. This coating is the main enabler for nucleation site control. Additionally, the ability to apply the coating in such thin layers permits large changes in wettability while making relatively insignificant changes to surface roughness.

A simple application of high temperature polyamide Kapton tape permits a small area of the surface to be shielded from the ALD process. This application is known as a mask. Hole-punches of different sizes are used to cut small circles from a 1 mil Kapton sheet. The Kapton circles are applied before ALD coating and peeled away afterward to leave the high contrast pattern of

wettability. The placement of the circles is done by hand. In order to ensure consistent placement, laser-cut paper stencils with concentric holes guide the user to place the circle in the correct location.



Figure 15 Photos of Coated Surfaces

After boiling, the ALD coating is stripped away by 20% nitric acid with light mechanical agitation. The acid solution is the same concentration used during passivation so it does not react with the already passive substrate. If the coating is stubborn or if there is residue, light sanding is used to remove it. Subsequent passivation is always performed before the next ALD coating. The resulting surface is hydrophilic with a circular hydrophobic spot in the center.

With each trial, the hydrophobic and nearby hydrophilic areas are characterized before and after boiling of the surface. The surface roughness is measured with a Veeco Wyko optical

surface profiler. Three measurements are taken within the hydrophobic area and three are taken just outside. These measurements are taken before and after the boiling experiment.

Table 2 shows the measured surface roughness in the coated and uncoated regions for each surface. The coated regions have a nearly constant surface roughness throughout the experiment. The roughness measurements have variability particularly in the uncoated region. Residue left behind from the Kapton tape is believed to be the source for variability in roughness in the uncoated areas. This adhesive is made from silicone and is highly temperature and chemical resistant. Therefore, the residue must be removed by mechanical means. However, mechanical agitation can affect the ALD coating. For these reasons, the residue is left on during boiling experiments. Figure 55 to Figure 62 in the appendix show the surface scans that indicate a residue on the hydrophobic regions of the surfaces.

Table 2 Average Roughness of Coated and Uncoated Regions

Surface	Ra (nm)	
	Uncoated	Coated
1	26.9	23.4
2	71.7	31.1
3	53.0	29.4
4	33.8	34.7

The surface's affinity for water, its wettability, is quantified using the sessile drop method with a KRÜSS DSA100 drop shape analysis system. Wettability is measured after the boiling experiment is concluded. A micro pipette is used to administer a deionized water droplet 1 to $3\mu L$. The drop shape analysis system records a photograph of the droplet in contact with the

surface. Contact angle is measured from the photograph using the ImageJ angle measurement function.

Table 3 Average Contact angle of Coated and Uncoated Regions

Surface	Contact Angle (deg)	
	Uncoated	Coated
1	71.2	54.6
2	54.5	20.5
3	84.8	22.7
4	99.2	53.9

Table 3 shows the difference in contact angle from the hydrophobic region to the hydrophilic region for each surface. There is also some variability in the contact angle measurements. However, in this case both the coated and uncoated regions show significant variability. This residue may also play a role in the wettability of the uncoated region. The source of variability in the coated region is not known. However, the aim of these surface modifications is to generate a surface with regions of high contrast wettability changes. The presence of this residue may introduce variability, but it likely adds to the contrast in wettability. Furthermore, there is always greater wettability in the coated regions than in the uncoated regions. It should also be noted that the two smallest spots required a reduction in droplet size. $1\mu L$ droplets were used for the smaller spot sizes and $3\mu L$ droplets were used on surfaces with larger spot diameters. Possible future studies with smaller spot sizes may not permit contact angle measurements as they become increasingly difficult to place a droplet within the decreasing spot diameter.

2.3.2 Varying Heater Area Surface Modification

For the study of varying heater areas, the possible nucleation area is relatively large, but needs to be limited to a single nucleation site. Furthermore, this study should compare the nucleation behavior of hydrophilic and plain surfaces. Therefore, a plain surface was modified in a specific order. First, a plain surface was sanded and passivated in the same manner as the previous study. The surface was then coated with 15nm of TiO_2 , in the same manner as the previous study. The heater was subsequently indented using a hardened steel scribe sharpened to approximately 19 degrees included cone angle. The optical comparator is indicated in Figure 16. The scribe was pressed into the coated surface with 10lbs of force.

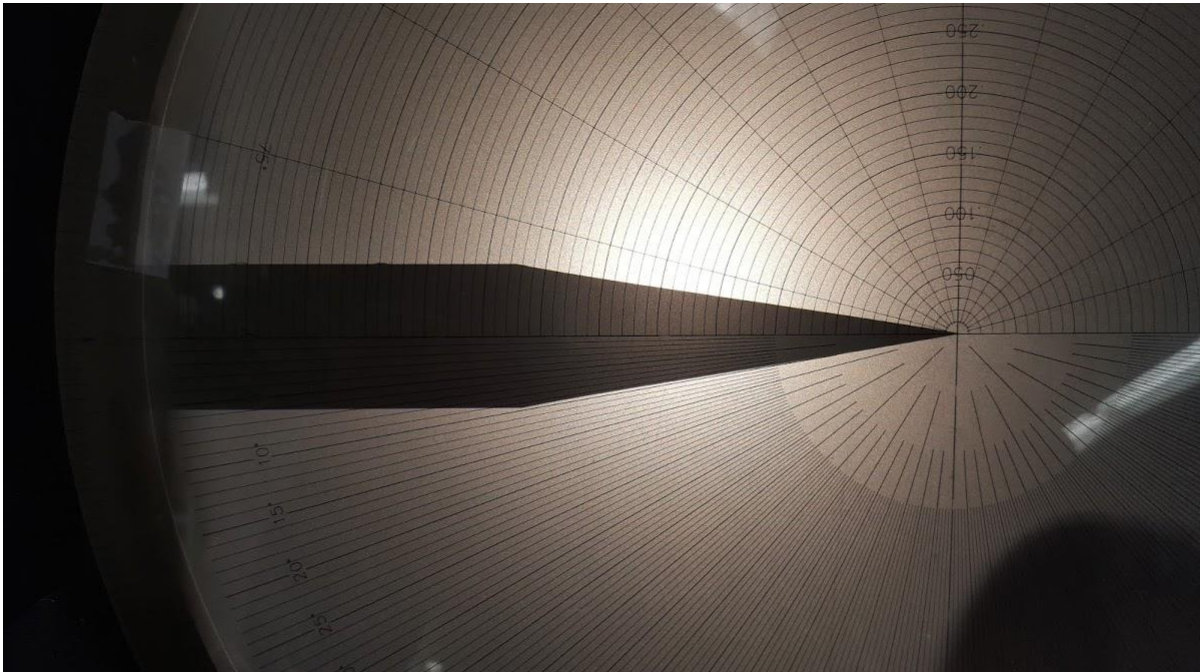


Figure 16 Image of Indenter Scribe Under Optical Comparator

The coated and indented surface is then cleaned and assembled for the first series of tests. After the testing of the coated surface is completed, the surface is stripped and passivated using 20% Nitric acid. The surface is once again assembled and tested with the bare, passivated stainless steel. This method ensures that the mechanical indent is not coated with TiO₂ and is not appreciably changed between runs. Therefore, if the indent is identical, then the variability must be attributed to changes in the flat surface; namely wettability.



Figure 17 Cartoon of Nucleation Site Indent With and Without Coating

The surface is removed after the boiling tests and is examined under a microscope. Figure 18 reveals that a second indent was also placed near the first indent. Although the second indent was not intended, it is close enough to not be considered part of the same nucleation site. The total width of the two indents is under 214 μm . Even in the highest frame capture rate there was no observed double-site behavior even at the very beginning of the bubble growth. Despite there being two indents, they are both considered to be part of the same nucleation site for the entirety of this study.



Figure 18 Image of Two Indents at 1000x Magnification

2.3.3 Thermal Effect of the TiO₂ Coating

The TiO₂ coating adds thermal capacity and changes thermal resistance of the surface. However, this effect is negligible as the following analysis will demonstrate. The largest diameter of the varying heater tip study is 9.52mm and the thickness of the coating is 15nm. With a density of 4050kg/m³, the mass of this volume is 4.33μg. With a specific heat of 697J/kg*K, the coating would require 90.5μJ to raise it a generous 30K. It is less than 0.2% of the latent heat required to create a single 3mm diameter bubble, 53.3mJ. The additional thermal resistance resulting from this layer raises the heater temperature as well. With a conservative thermal conductivity of 4.8W/m-K and a conservative heat flux of 10⁶W/m², the additional rise

in temperature of the hot side of the surface would be 0.00312K. Therefore, the conductive effects of the 15nm TiO₂ coating are safely considered to be negligible.

2.4 EXPERIMENTAL PROCEDURE

After surface modification and characterization is performed, the surface is assembled into the boiling apparatus. The surface heater is assembled with the thermal interface material. The mass of the thermal interface material is measured and recorded. The force gauge is zeroed and the force measurement and adjustment feedback system is initiated. In the case of the varying heater tip study, the thermal interface material is applied liberally and the excess is brushed away after assembly. Ice is packed in the thermocouple reference junction wells. Deionized water is used to fill the boiling apparatus. Condenser lines are connected and tap water is supplied to the system. Local pressure and temperature is subject to changes dictated by the building heating ventilation and air conditioning system, but only affects the reflux condenser performance.

Hysteresis is known to occur with boiling experiments due to continually changing surface geometry and chemistry from boiling deposits. Therefore, it is standard convention to increase heat flux in small increments but never to decrease heat flux until termination of the experiment. A typical increment for this experiment is 1 kW/m² although one series has a much larger increment of roughly 5 kW/m². For low heat fluxes, many steps may occur before boiling is observed. Therefore some of this data may be rejected or deleted. Bubbles will continue to be produced within the hydrophobic area until it can support no further vapor generation. Once bubbles begin to grow and depart from the hydrophilic region, the experiment is concluded and the power is no longer supplied.

In the case of the varying heater diameter study, each surface is used for multiple trials. However, those trials are conducted in order of largest heater to smallest and, in general low heat flux to high. Each trial has two or three heat fluxes tested; ONB, middle (if applicable) and the highest heat flux the setup heater can safely produce.

2.5 IMAGE ANALYSIS

2.5.1 Convention for Image Post Processing

Visual examination of bubble behavior with a high speed camera offers a different way to explore the effects of bubble growth and departure. The main parameters of interest are bubble departure frequency and bubble departure diameter. Bubble departure frequency is measured by counting the number of qualified departures and dividing by the time interval over which they were counted. The bubble departure diameter is approximated by measuring the widest point of the bubble on the last frame before the bubble detaches from the surface. This diameter is adjusted according to the relation outlined in the next section. Figure 19 shows how bubble departure shape can vary even for a single site. There is often more than one bubble present during the ebullition cycle and coalescences may perturb the bubble. Indeed, the bubble on the right hand side of Figure 19 is experiencing coalescence with smaller feeder sites that are likely responsible for some of the distortion.

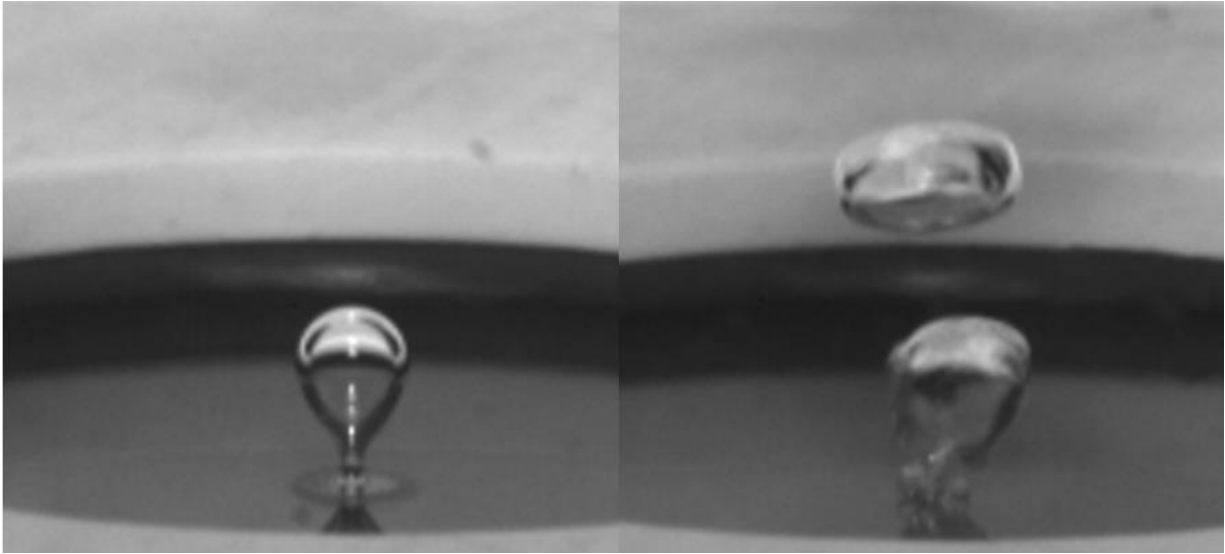


Figure 19 Contrasting an Unperturbed Bubble with a Perturbed Bubble

Vertical, declining and horizontal coalescences are other secondary parameters of interest. These parameters are less straight-forward to define than the previous parameters. Vertical coalescence is defined as two consecutive bubbles from the same nucleation site that coalesce together. More specifically, when the second bubble grows so quickly that it contacts and coalesces with the previous bubble before its own departure, it is qualified as a vertical coalescence. Figure 20 illustrates a typical vertical coalescence. In the second image, the growing bubble makes contact with the previous bubble. The third and fourth images show where the two boundaries of the bubbles begin to join to make a single boundary. The subsequent images show the flow of vapor from the lower bubble into the upper bubble, completing the coalescence.

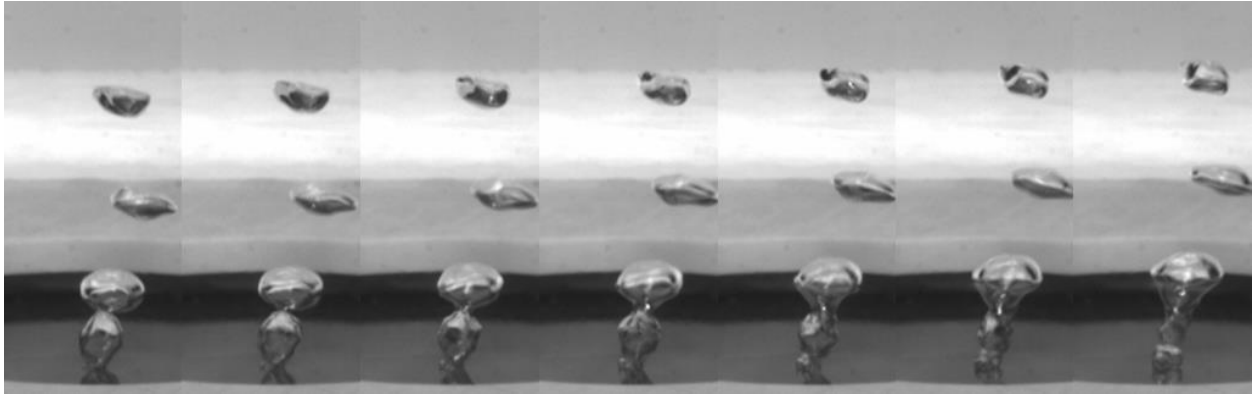


Figure 20 Illustration of Vertical Coalescence 0.001s Time Step

Declining coalescence is when two adjacent nucleation sites produce bubbles that coalesce in a particular way. When a bubble coalesces with an adjacent and previously-departed bubble before its own departure, it is qualified as a declining coalescence. Figure 21 shows two bubbles near the heated surface. The bubble on the left has already departed while the bubble on the right is still attached to the surface and growing. The second image shows the merging of their boundaries. The fourth image shows the second bubble detach as it continues its coalescence. The subsequent images show the bubble shape tending toward a sphere as it rises in the water.

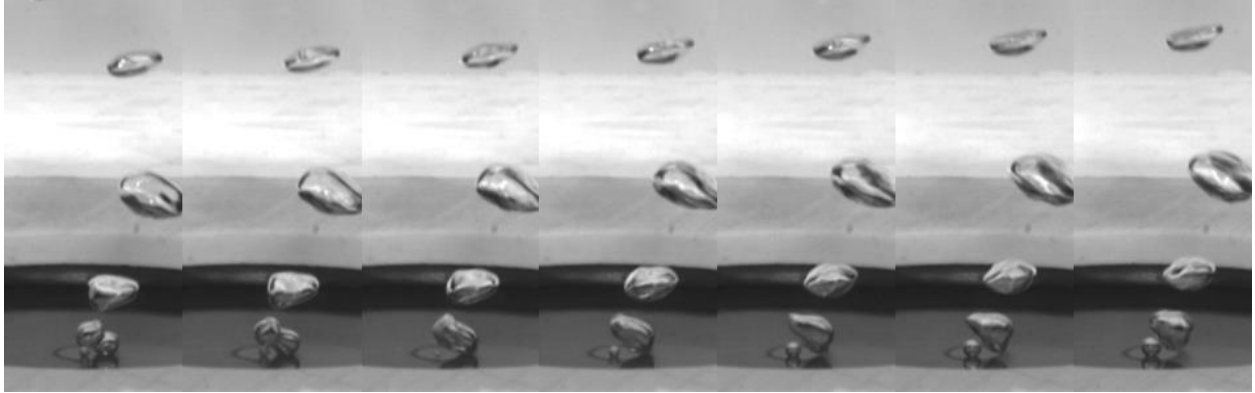


Figure 21 Illustration of Declining Coalescence 0.001s Time Step

Horizontal coalescence is similar to declining coalescence, except both bubbles must coalesce before departure. These coalescences are the rarest of the three types identified. Furthermore, even though two bubbles experience the coalescence, only one coalescence is credited for the purposes of counting. The frequency of these different types of coalescences is measured in the same manner as departure frequency. Figure 22 shows a pair of bubbles of similar size growing together. The fourth image shows their boundaries joining. The subsequent images show the resulting deformations, but do not show the final bubble departing.

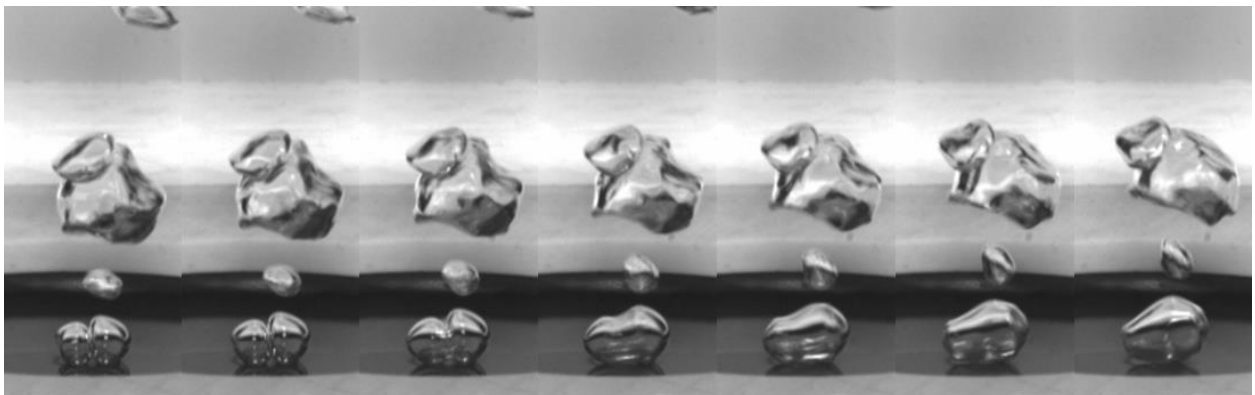


Figure 22 Illustration of Horizontal Coalescence 0.001s Time Step

It is important to note that not every instance of bubble coalescence is counted. There are some cases where feeder sites are responsible for the majority of a bubble's growth. Bubbles growing from feeder sites are assumed to be part of the main nucleation site. A feeder site is identified as a nucleation site that generates a small bubble that joins with the main bubble. These feeder bubbles are typically generated at high frequency and are often so distorted that a diameter measurement is impractical. These sites are incapable of generating independent bubbles on their own due to their proximity to a more dominant site or that their growth time is so long that they are more likely to be absorbed than to depart on their own. Figure 23 shows a few instances of feeder site growth and coalescence. Images 1, 2, 3, and 7 all show a feeder site to the left of the main nucleation site. These images are taken at 1000 frames per second. However this speed is not fast enough to positively state that these feeder sites have not coalesced and regrown between frames. Conversely, because these sites are known to be unable to produce an independent bubble departure, they are simply considered to be part of the main bubble growth.

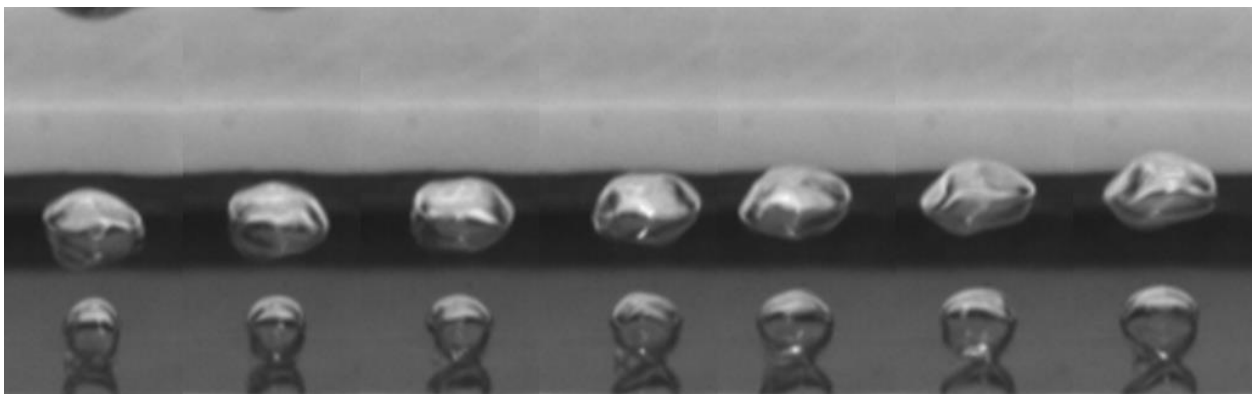


Figure 23 Illustration of Feeder Nucleation Sites 0.001s Time Step

It is important to note that coalescence that occurs away from the surface is not considered. As the knowledge of heat transfer is of primary importance, behavior that happens away from the heated surface is less likely to impact the behavior at the surface. Therefore, measurements of bubble behavior are performed only if one or more of the bubbles are touching the surface.

2.5.2 Determining the Volume of a Bubble Using the Disc-Stacking Method

The volume of a bubble is a necessary component for determining the rate of latent energy conversion. This section will explain the more in-depth bubble volume estimation method which will reveal information used in simpler estimations. In the analysis of a single growing bubble, the shape of the bubble begins short and wide but departs with an elongated shape. For these reasons, the width of a growing bubble was assumed to be unsuitable for estimating the bubble volume as a function of time. Therefore, a disc-stacking method was used to better approximate the volume of the bubble as it changed shape. Once the outline of the bubble is known, the method is simple. The bubble is naturally broken up into horizontal lines of pixels governed by the resolution of the image. Each line is a disc whose diameter corresponds to the length of the line in horizontal pixels and whose thickness corresponds to the height of one pixel. Figure 24 shows a bubble during various times of its growth.

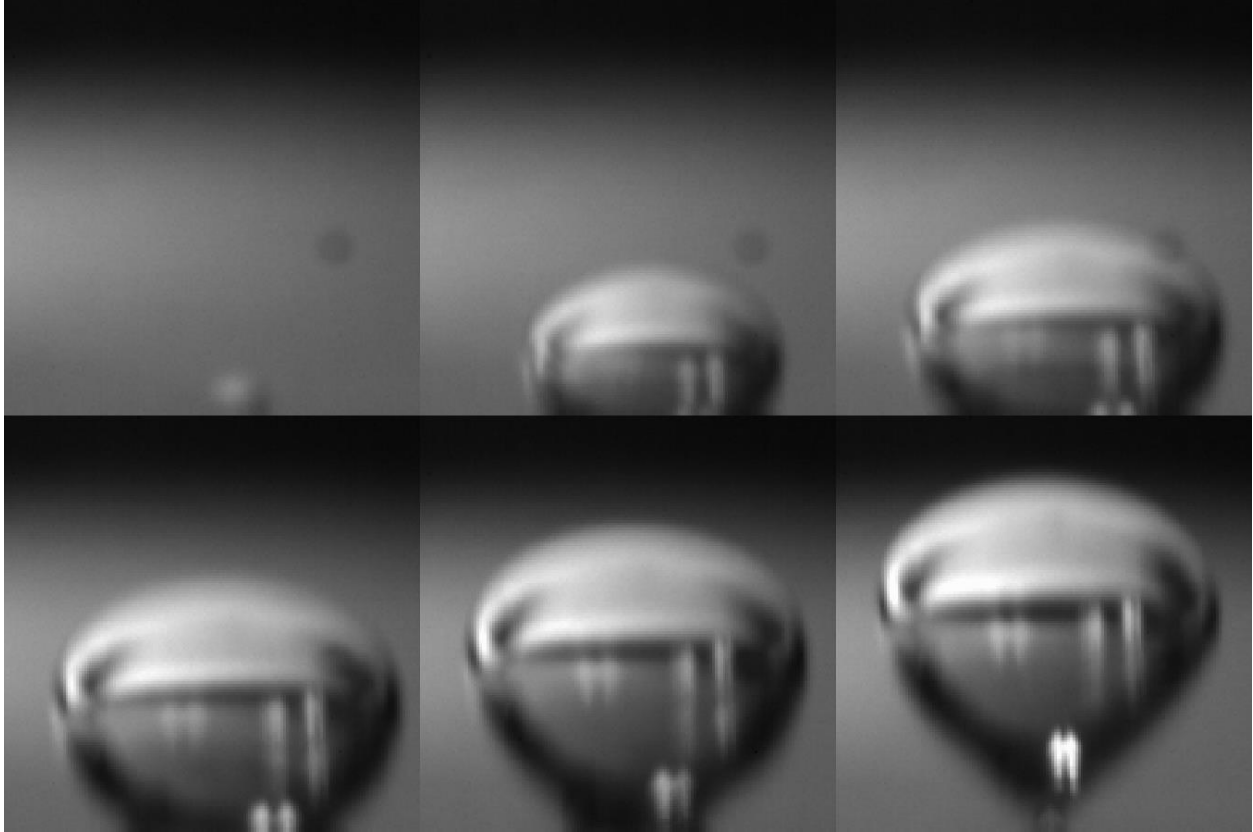


Figure 24 Image of Growing Bubble at $T = 0.1\text{ms}, 1.7\text{ms}, 3.5\text{ms}, 6.9\text{ms}, 10.4\text{ms}, 13.7\text{ms}$

Indeed, the bubble dimensions do not scale with time. The bubble begins wide and short but elongates during its growth. However, using the width of the bubble always results in an overestimation of volume. The equivalent diameter is the diameter of a sphere with the same volume as the bubble. Equation (7) displays this relationship mathematically.

$$D_{eq} = \sqrt[3]{\frac{6V}{\pi}} \quad (7)$$

Consequently, the bubble width is always greater than the equivalent diameter. Figure 25 demonstrates this behavior by plotting the equivalent diameter and bubble width against time. The starred points correspond to the images in Figure 24.

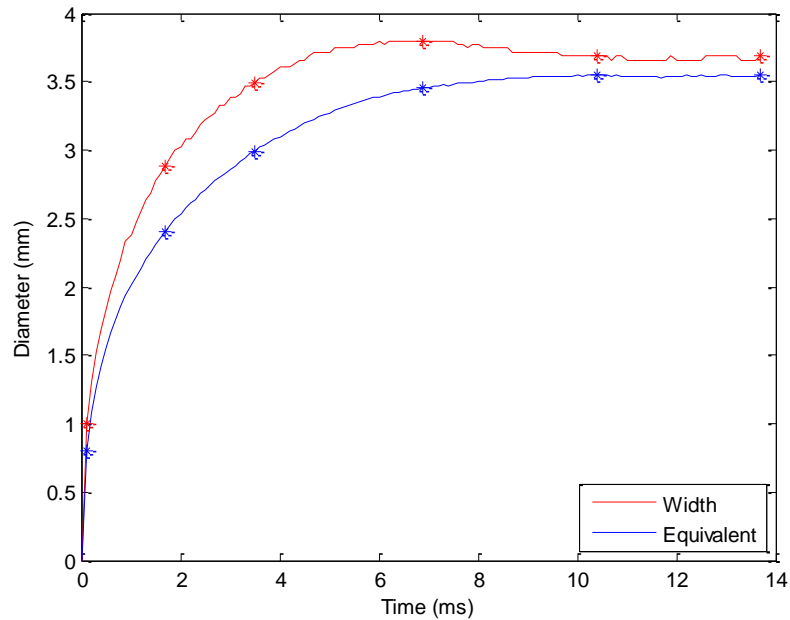


Figure 25 Comparison of Equivalent Diameter and Bubble Width During Bubble Growth

2.5.3 Approximating the Volume of a Bubble Using Its Width

The departure width is only a slight overestimation when compared to the equivalent diameter. The bubble width approximation has been shown to be problematic for time varying bubble geometry. However it may be suitable for approximating bubble departure volume. For the study where the disc-stacking approximation was used, each trial was used to compare equivalent departure diameter and departure width. One outlier was omitted. Figure 26 shows that the overestimation of the spherical approximation using bubble width increases with bubble volume.

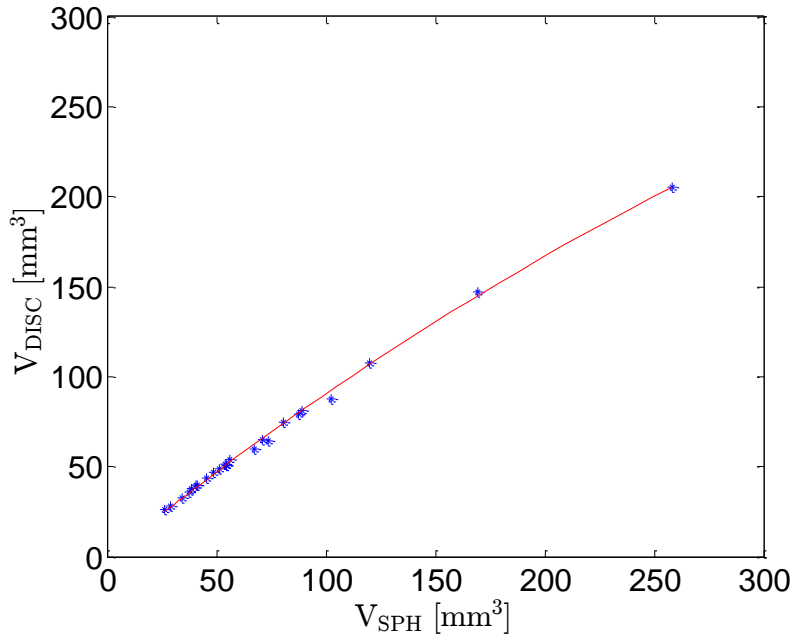


Figure 26 Overestimation of Volume by Spherical Approximation as a Function of Spherical Volume

A quadratic polynomial is fitted to the data. The adjusted volume can be computed according to Equation (8) where bubble width, V_{sph} and adjusted volume, V_{adj} , have units of cubic millimeters.

$$V_{adj} = -6.86E-4 \cdot V_{sph}^2 + 0.972 \cdot V_{sph} \quad (8)$$

This relation is used for trials where only departure geometry is of interest. It saves time in post processing and is easy to implement.

3.0 VAPOR GENERATION OF TEST SURFACES

Two sets of boiling surfaces are evaluated. A plain surface is coated with various biphilic patterns and is evaluated for multisite performance. A surface with a mechanical nucleation site is evaluated with and without a 15 nanometer thick hydrophilic coating by examining the single-site response to varying heater diameters. Three explorations are performed; multi-site sequence study; single-site sequence study, and single-site growth study. The main parameter for evaluating the performance of these surfaces is vapor effectiveness. Vapor effectiveness, E_V , is the ratio of latent energy conversion to the heat input supplied by the heater. Equation (9) defines vapor effectiveness in terms of vapor volume production rate, \dot{V} , vapor density ρ_v , and latent heat of vaporization h_{fg} , heat flux, q'' , and heated area, A_h .

$$E_V = \frac{\dot{V}\rho_v h_{fg}}{q'' A_h} \quad (9)$$

For the purposes of multi-site explorations, a second term called superficial vapor effectiveness is used. Superficial vapor effectiveness, SE_V , is the vapor effectiveness of each nucleation site on a surface if the other nucleation sites are not generating vapor. For the sake of simplicity, superficial vapor effectiveness will be defined as the vapor effectiveness divided by the number of active nucleation sites, n_s . Equation (10) illustrates this relationship.

$$SE_V = \frac{E_V}{n_s} \quad (10)$$

Superficial vapor effectiveness is used in order to make a more direct comparison of the performance of the individual site. For example, a nucleation site performs at 50% vapor effectiveness on a given surface. If another identical nucleation site appears on the same surface with the same heating conditions, the vapor effectiveness becomes 100%. However, the superficial vapor effectiveness still remains at 50%. This is an important distinction for the multi-site discussion. It is implied that in a multi-site configuration the total vapor effectiveness is equal to the superficial vapor effectiveness multiplied by the number of nucleation sites. This permits a more valuable comparison between the multi-site cases and the single site cases on the same surface.

3.1 MULTI-SITE BUBBLE SEQUENCE STUDY

From the study by Zhang and Shoji [9], we know that the three influences of bubble departure frequency are hydrodynamic, thermal (conduction), and coalescence. The present study focuses on vapor effectiveness instead of departure frequency as the main measure of performance for multi-site bubble interaction. Of the six surfaces examined, only the four surfaces with the largest hydrophobic spots exhibit multi-site behavior. The 3.18mm hydrophobic spot surface produces the highest number of two-site nucleation. It is also the only surface to produce three nucleation sites simultaneously. The superficial vapor effectiveness of each multi-site case is explored to reveal relationships to key parameters.

As the distance between nucleation sites increases, the improvement of average double-site superficial vapor effectiveness compared to average single-site vapor effectiveness increases.

This is intuitive because sites that are closer are more likely to share one another's thermal energy by way of conduction through the substrate.

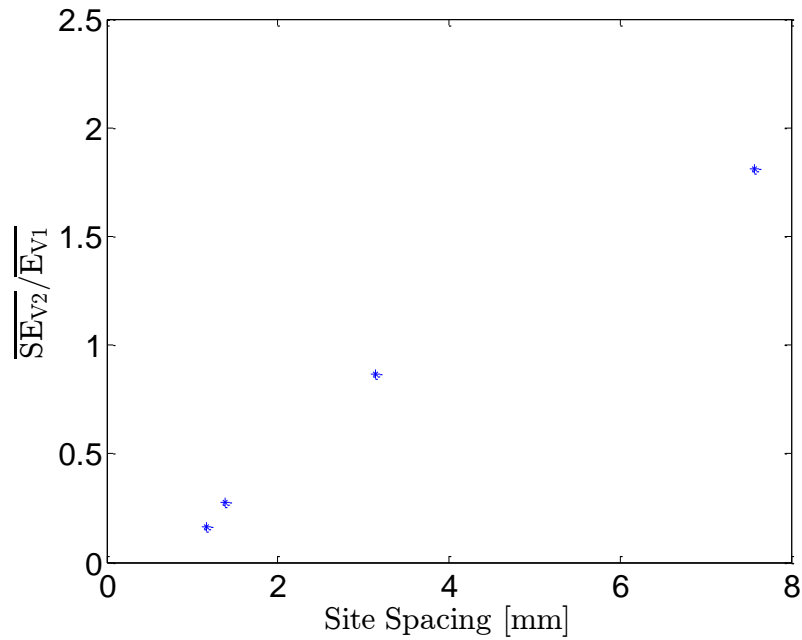


Figure 27 Comparison of Average 2-Site Superficial Vapor Effectiveness to Average 1-Site Vapor Effectiveness as a Function of Site Spacing

Conversely, sites that are further away may see the benefits of hydrodynamic or coalescence effects that are seen in Shoji's study [9]. It is expected that the ratio would approach 1 as the two sites become completely isolated. The results seen in Figure 27 do not observe the steadying at a ratio of 1. This is due to insufficient space between nucleation sites. However this trend suggests that a pair of bubbles spaced closer than 3.15mm already begin to lose the doubling benefit of two sites. Moreover, the average pair of sites that is spaced closer than approximately 2mm is expected to produce less vapor combined than the average single site in similar conditions (due

to the ratio being below 0.5). The fact that the double-site can actually produce less vapor than the single site means that there are effects beyond the sharing of the thermal energy in the substrate or the superheated layer. The presence of the second bubble is perturbing some mechanical behavior other than the heat supply in the substrate. Possible explanations include the effect of coalescence or hydrodynamic effects.

Bubble coalescence is divided into three categories; vertical, declining and horizontal. These coalescences are measured in units of frequency and are compared to vapor effectiveness. The study by Zhang and Shoji [9] asserts that coalescence has a promotive effect upon bubble departure frequency. However, the current study finds that superficial vapor effectiveness is affected little or none by coalescence as shown in Figure 28. Each case occurs on the same surface. The single-site cases are grouped and averaged. The double-site cases are examined for coalescence frequency and are individually compared to the average of the single site case. The bubbles in the double-site cases are all spaced 3.15mm apart. Only the cases with 3.15mm spacing are presented here to maintain a consistent approach.

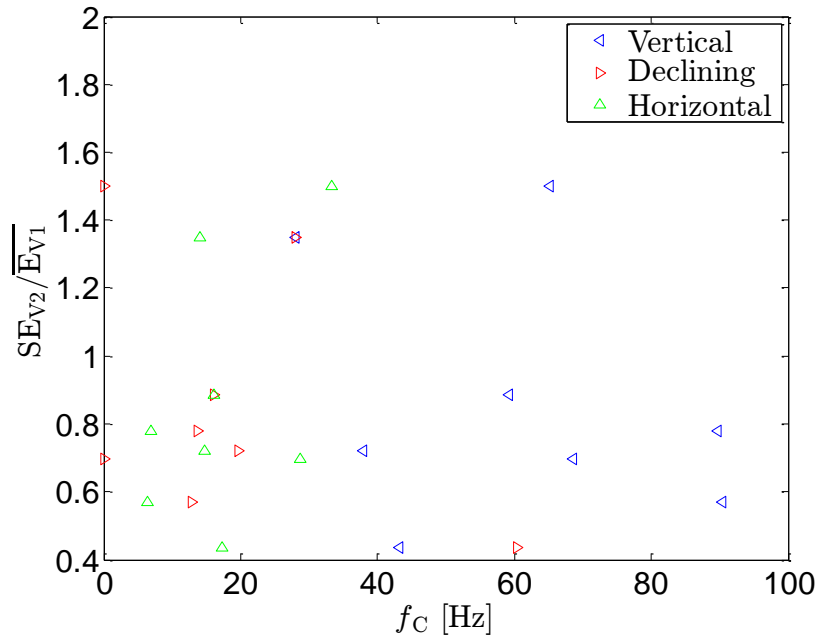


Figure 28 Comparison of Coalescence to Superficial Vapor Effectiveness Ratio from Double Site to the Average Single Site. Double Sites spaced at 3.15mm.

None of the three types of coalescences appear to have a discernable effect upon vapor effectiveness. At the very minimum, horizontal coalescence is expected to have some effect upon vapor effectiveness as it causes a shift of the base of the bubble along the heated surface. However, if there is an influence, promotive or inhibitive, it is not clearly observed in this study. There is a wide spread in the data that, in terms of coalescence, appears to be random error. The role of coalescence in vapor effectiveness is, therefore, ruled out. However, the next investigation shows the spread is due to other, stronger influences.

Hydrodynamic influences are best described as perturbations in the fluid field surrounding a bubble that affect its thermal performance. In pool boiling, hydrodynamic effects arise primarily because of bubble wakes. In the single site regime, hydrodynamic effects are responsible for sweeping up the superheated layer beneath a bubble and depositing a small pocket of

superheated liquid directly above the nucleation site prior to the next bubble ebullition. A study by Yakubi and Nakabeppu [8] illustrates this superheated pocket by use of interferometry. The wake of a previous bubble can also affect the force balance on a growing bubble. In the two-site regime, hydrodynamic effects may shift the superheated fluid in the adjacent site. Furthermore, the wake of a departed bubble asymmetrically alters the force balance on an adjacent growing bubble. Shoji's study [9] identifies hydrodynamic effects as promotive for departure frequency enhancement. In this case, the two main variables driving hydrodynamic effects are velocity and bubble geometry. Figure 29 plots bubble departure velocity against superficial vapor effectiveness for the 3.175mm spot series. For single nucleation sites, there is a strong relationship between bubble departure velocity and vapor effectiveness. However, this relationship is weaker and more varied for double and triple nucleation sites.

One possible explanation of this degradation of velocity influence is the displacement of the superheated pocket into a configuration less favorable for phase conversion. Another explanation is that the perturbation of a growing bubble may cause it to detach earlier than it would in a quiescent environment. This behavior requires further investigation.

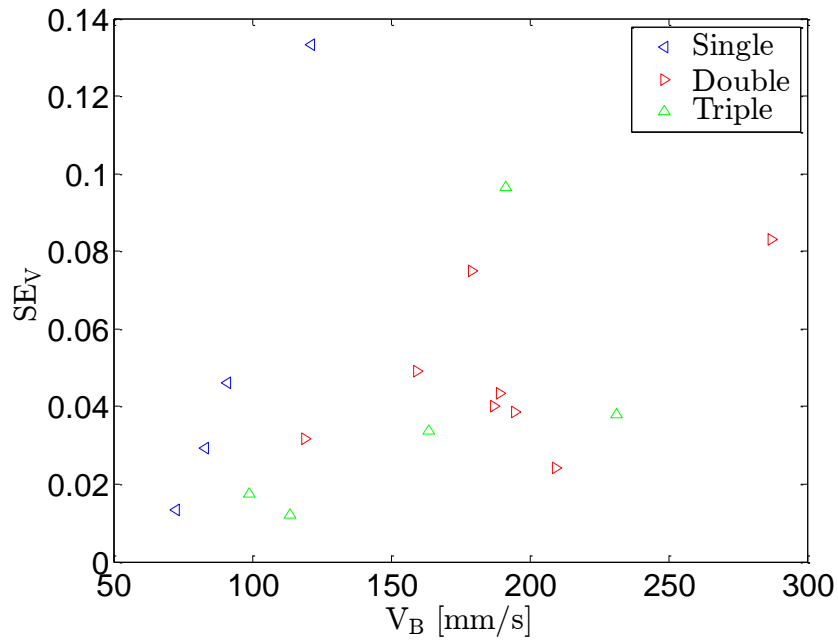


Figure 29 Comparison of Average Bubble Velocity and Superficial Vapor Effectiveness for Single, Double and Triple Site Configurations

The next exploration into multi-site vapor effectiveness is bubble diameter. For the purposes of bubble departure frequency, site spacing is usually normalized by bubble diameter. However, for the purposes of vapor effectiveness, the exploration of bubble diameter as a separate parameter yields interesting results. In Figure 30 each trial is performed on the same surface with heat flux being the only variable changed between runs. For each of the single, double and triple cases, the bubble diameter is positively correlated with vapor effectiveness.

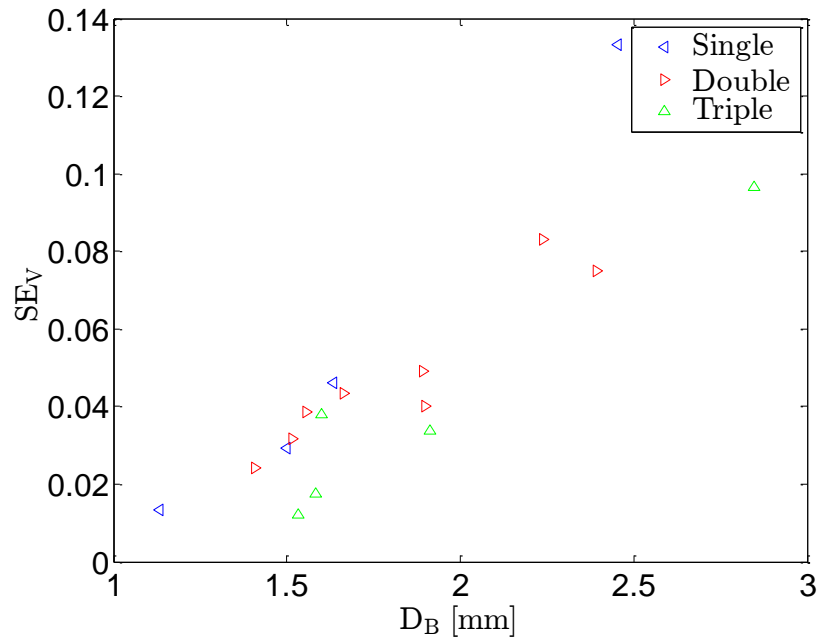


Figure 30 Comparison of Average Bubble Diameter and Superficial Vapor Effectiveness for Single, Double and Triple Site Configurations

The single site has the strongest relationship, but the double and triple site relationships are still strong, unlike the trend with velocity. The possible explanations for the influence of the bubble diameter are numerous. One of the most intuitive considerations is that larger bubbles have more interface area which offers a better opportunity to convert liquid superheat energy to latent energy. The larger the growing bubble becomes, the more exposure any superheated layer or pocket has to the bubble interface.

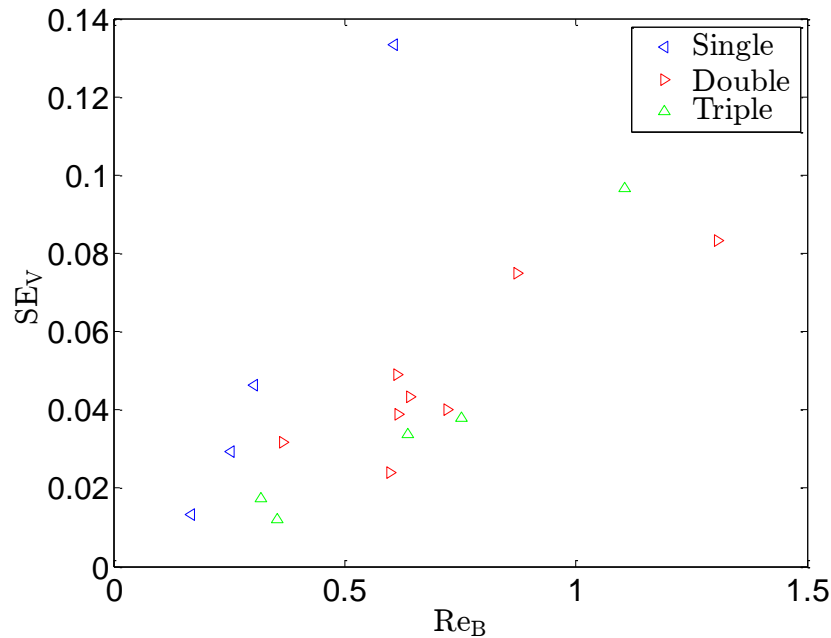


Figure 31 Comparison of Average Bubble Reynolds Number and Superficial Vapor Effectiveness for Single, Double and Triple Site Configurations

A more concise metric of the hydrodynamic effect is the Bubble Reynolds number. This dimensionless group credits both velocity and bubble diameter. Indeed, the Bubble Reynolds number indicates the same hydrodynamic trends seen in bubble diameter and bubble velocity. The hydrodynamic effects indicated by higher Bubble Reynolds numbers are shown to positively affect single site vapor effectiveness but those benefits are less dramatic for the multi-site cases. The hydrodynamic effect of larger, faster bubbles is therefore unlikely to be the only cause for improvements in the multi-site cases. And finally, the conductive thermal effect is logically assumed to be a prohibitive factor. Larger bubbles absorb more heat from the substrate, thereby increasing the size and magnitude of the cold spot beneath a nucleation site. It is highly unlikely that any effect of the larger bubble in the substrate conduction contributed to the effectiveness enhancement.

This multi-site study showed that the majority of multi-site cases performed worse, on average than a single site. However there are several ways to improve vapor effectiveness with the multiple sites. The major findings are that wide nucleation site spacing and large bubbles contribute to an effective vapor-producing boiling surface. High bubble departure velocity does correspond to improved single-site vapor effectiveness but the effect diminishes for the multi-site scenario. It is suggested that this is caused by an asymmetric perturbation of the superheated pocket above a nucleation site. Figure 32 illustrates the formation and subsequent displacement of the superheated pocket. Step A shows two bubbles growing with the bubble on the left about to depart. Step B shows the departed bubble gathering the superheated pocket as suggested by Yabuki and Nakabeppu [8] and previously indicated in the reproduction of their image in Figure 2. Step C shows the superheated pocket from the left bubble being drawn toward the departing bubble on the right due to its wake. Finally, step D shows the remaining superheated pocket being shed away from the bubble rather than contributing to more latent energy conversion at its surface, thus resulting in suboptimal vapor effectiveness.

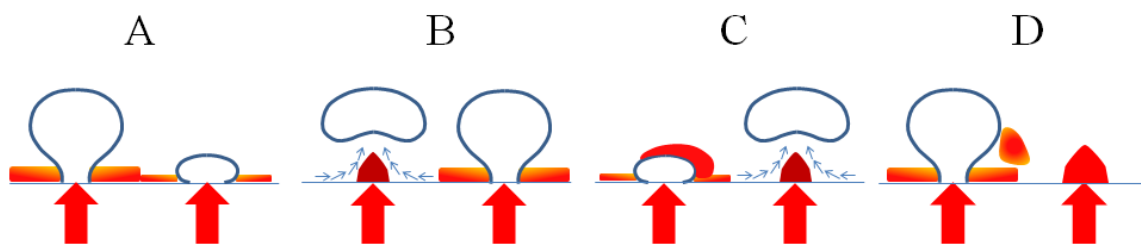


Figure 32 Cartoon Illustration of Displacement of Superheated Liquid Pocket Resulting From Nearby Nucleation Site

The displacement of this pocket of higher energy liquid could make the bubble less likely to convert it to latent energy. However, larger bubbles may be more tolerant of this displacement as they have more interface area to convert sensible energy to latent energy. Wider site spacing also mitigates this effect.

3.2 SINGLE-SITE BUBBLE SEQUENCE STUDY

In the case of single site bubble effectiveness, the heated area is the most obvious parameter of interest. The heated area under a nucleating bubble can dissipate its heat in 3 ways; sensible heating of the superheated thermal boundary layer, heating of the microlayer that results in phase change at the liquid-vapor interface and sensible heating of the vapor in contact with the dry spot. Radiation participation is negligible for nucleate boiling or low superheats. Figure 33 illustrates three regions where the different routes for heat dissipation would be expected to operate. In terms of vapor production, region three can only contribute to vapor production while the bubble is small enough to be enveloped by the thermal boundary layer. However, the majority of the heat dissipated in region 3 will diffuse into the bulk fluid. In the case of saturated bulk fluid, such as in this study, Region 3 will not contribute to vapor generation unless the bubble interface is in contact with the superheated thermal boundary layer or if there is displaced superheated liquid touching it. If the bulk fluid is subcooled, the bubble interface in contact with it may allow the vapor to condense. Region 2 is where the majority of the phase change heat transfer occurs. Conduction through the micro and macro layers drives evaporation at the liquid-vapor interface. The triple contact line is the circular line where solid, liquid and vapor are all in contact. Inside this line, only vapor contacts the solid surface. This area is known as the dry spot

and heat transfer only occurs in the form of superheating of the vapor in an ideal system. However, radial conduction in the substrate could contribute to heating in region 2, and subsequently vapor production.

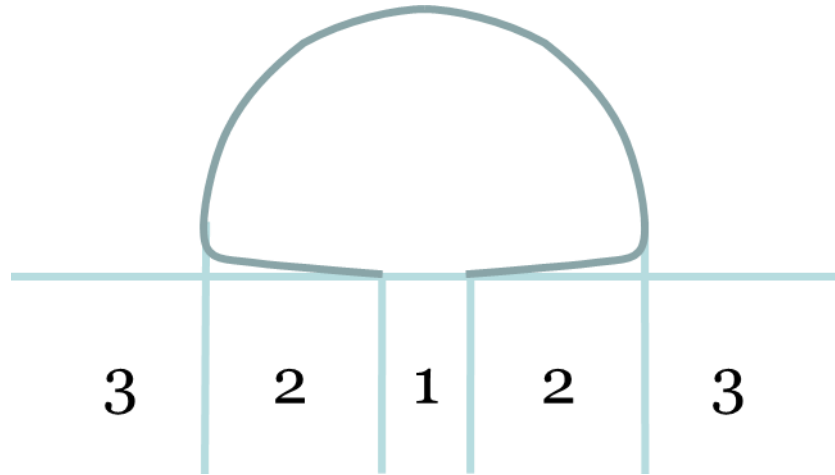


Figure 33 Cartoon Illustration of Three Paths for Heat Transfer Out of Solid

The present study attempts to constrict the heat supply to regions one and two. This will reveal the effects of two competing processes; reducing sensible heat lost radially into the bulk fluid and reducing heat transfer through the micro and macro layers. This is accomplished by delivering measured heat to a thin, stainless steel substrate with heater and caps of varying contact diameter. On the boiling side of the substrate, bubble performance is measured with a high speed camera.

Constricting the heat supply to a small area surrounding an artificial nucleation site does have one main limitation. The heat flux at a small heater diameter must be much greater for the onset

of nucleate boiling to occur. Figure 34 demonstrates the necessary heat flux to achieve the onset of nucleate boiling for varying heater diameters.

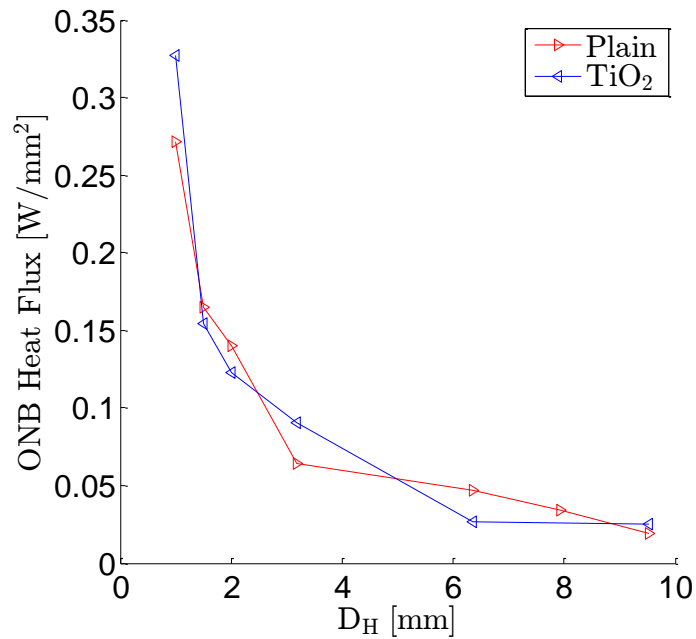


Figure 34 Graph Showing Increased Heat Flux Required For Onset of Nucleate Boiling With Reduced Heater Diameters

However, the benefit of the smaller heater diameter is the reduced heat input required to generate bubbles. Figure 35 demonstrates the reduction in heat required to initiate boiling.

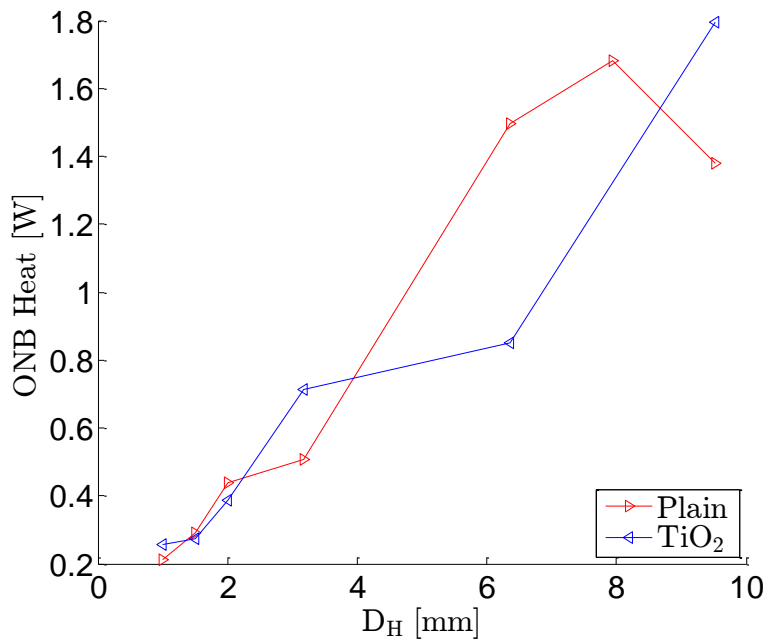


Figure 35 Graph Demonstrating Increased Heat Transfer Required for Larger Heaters

The remainder of this section quantifies the vapor effectiveness and identifies mechanisms responsible for this behavior. The results of the multi-site study found that evaporation of the thermal boundary layer was likely contributing to higher levels of vapor effectiveness. The present study dramatically reduces the area over which the heat is transferred and is therefore reducing the likelihood of this layer forming. Instead, all of the heat is being transferred directly under the bubble or slightly beyond it. Therefore, the mechanisms that drive the effectiveness increase in the multi-site study should play little or no role in the present study. The mechanisms were identified as increased bubble diameter exposing the interface to more superheated fluid and higher bubble velocity which draws more superheated liquid beneath the departed bubble which feeds the growth of the bubble about to begin growth in a new ebullition cycle. Therefore, the single-site study with constricted heater diameters should vary in effectiveness independent

of bubble diameter or velocity. Figure 36 illustrates that there is no strong correlation between Bubble Reynolds number and bubble effectiveness.

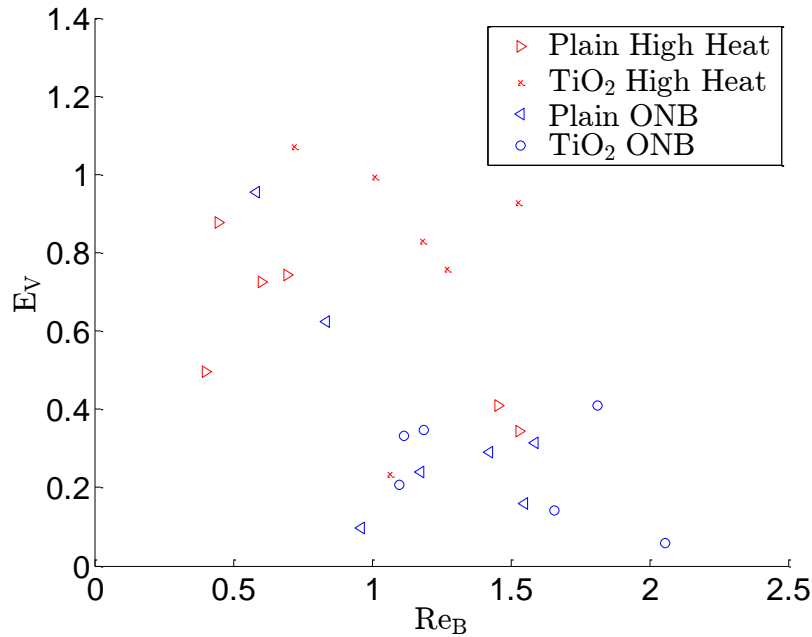


Figure 36 Graph of Bubble Reynolds Number and Vapor Effectiveness

This finding further supports that the hydrodynamic influence is likely due to the presence of a considerable superheated thermal boundary layer. Furthermore, the relationship between these parameters became weaker when competition from other sites was present. This suggests that there is a mechanism separate from Zhang and Shoji's [9] H, T and C mechanisms involving the evaporation of the superheated layer. While the bubble velocity and diameter involvement in vapor effectiveness would likely fall under a hydrodynamic classification, their effect is not strictly promotive as suggested by Shoji. Indeed, while in the single site regime, they serve to

improve effectiveness, however in the multisite regime, the increase of bubble diameter and velocity increases the sharing of thermal energy in the superheated boundary layer. The implication of this finding is that the inhibitive effects of bubble cross-talk in multi-site nucleation may be mitigated by constricting the flow of heat to directly beneath each nucleation site only. This would permit bubbles to grow without competing for heat within the superheated layer and possibly heat within the substrate. The limits of the other promotive aspects of bubble interaction, hydrodynamic and coalescence, could be more fully explored without the inhibitive effects of cross-talk within the thermal boundary layer.

Some of the smallest and slowest departing bubbles yield the highest vapor effectiveness in the single site regime with small heater diameters. Therefore, the mechanisms contributing to vapor effectiveness are different for bubbles generating from surfaces with constricted heater area. In Figure 37, vapor effectiveness is shown to have a strong dependency upon heater diameter. In general, vapor effectiveness steadily increases with decreasing heater diameter until a slightly sharper increase near 2mm and a very sharp decrease at a lower limit. In 2015 Jung and Kim [39] measured a dynamically changing microlayer diameter and dry spot diameter. The maximum microlayer and dry spot diameters were 2.3mm and 1.2mm, respectively. This study is relevant to the present study because a heater that is smaller than the microlayer outer diameter will not lose heat into region 3 from Figure 33 which is favorable for vapor effectiveness. Similarly a heater that is smaller than the dry spot diameter will only supply heat into region 1 which is unfavorable for vapor effectiveness.

In Figure 37 there are two vertical, dotted lines representing the values published by Jung and Kim [39]. Below the published maximum microlayer diameter of 2.3mm, there is a stronger increase in effectiveness for both the plain and coated sites. However, there is a sharp decrease in

vapor effectiveness for heater diameters below the published maximum dry spot diameter of 1.2mm. Indeed, at some point during the growth, the smallest heater might be covered with vapor. In this case, some sensible heat would raise the temperature of the lower conductivity vapor, while the rest is conducted outward through the substrate to supply heat to the triple contact line and the liquid in the microlayer. The sensible heating of the vapor is substituted for latent heating and, thus is responsible for the lower vapor effectiveness of the smaller heater diameters. The trend of vapor effectiveness for heater diameters above the maximum dry spot diameter requires further explaining.

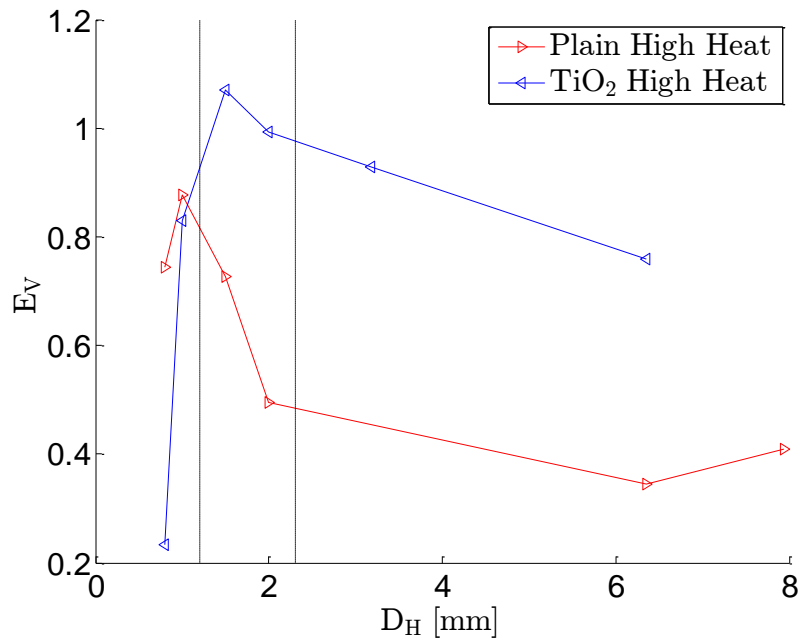


Figure 37 Comparison of Heater Diameter and Vapor Effectiveness

While the microlayer can be several millimeters wide, it is very thin in comparison to other length scales of interest. Jung and Kim measured the maximum thickness of the microlayer to be roughly 3 microns at its outermost point and linearly decreasing to zero where it meets the triple contact line. Heat transferred into this microlayer slightly superheats the liquid where it then evaporates at the bubble surface. By reducing the heater diameter smaller than the microlayer diameter, sensible heat that would normally be conducted radially away from the bubble now has to travel through the microlayer. See Figure 38 for reference.

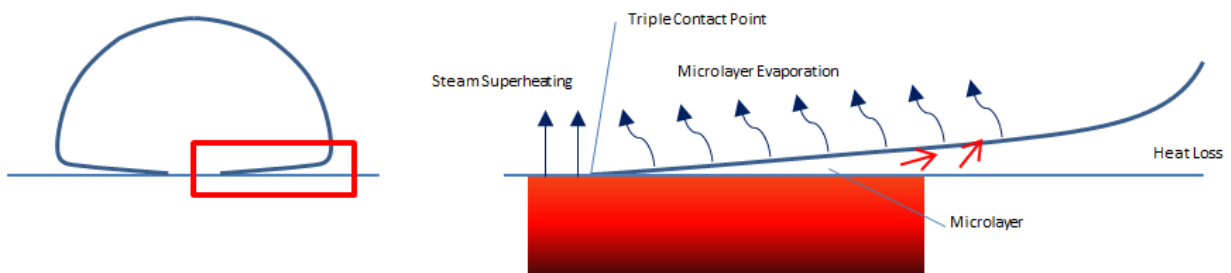


Figure 38 Diagram of Heat Flow Near the Microlayer

This heat is more likely to be converted to latent heat than if it were traveling through the thicker layer of liquid outside the microlayer. So there is a separate mechanism for increasing vapor effectiveness once the heater is smaller than the microlayer. By reducing the diameter of the heater, there is less circumferential area for heat loss. Furthermore, for heaters below the microlayer diameter, heat diffusing radially from the heat source must travel through the very thin microlayer which is favorable for phase conversion.

One interesting observation from Figure 37 is that the surface coated with titanium oxide performs better overall than the uncoated surface. It may be tempting to attribute this benefit to the larger bubble diameters produced by a wettable surface, but the earlier part of the present study suggests that bubble diameter has no effect on surfaces with small heater areas. However, surface wettability also affects contact angle and likely affects the thickness of the microlayer and, therefore, may delay the maturation of the dry spot.

The highest vapor effectiveness reported in this series is 107%. This shows that there is either an over-prediction of the latent energy conversion or an underprediction of heat flux. In either case, each trial was performed with the same instruments, methodology and post-processing techniques. So, the trends in vapor effectiveness are still useful for the microlayer discussion.

Normalizing the heater diameter with respect to the bubble diameter reframes the discussion. If the microlayer is larger for larger bubbles, then normalizing the heater diameter with respect to the bubble diameter may reveal the reason for the difference. Figure 39 shows that the trends between the two surface coating configurations behave differently. The difference may be because the microlayer geometry for a wettable surface is thicker or otherwise more favorable for effectively producing vapor.

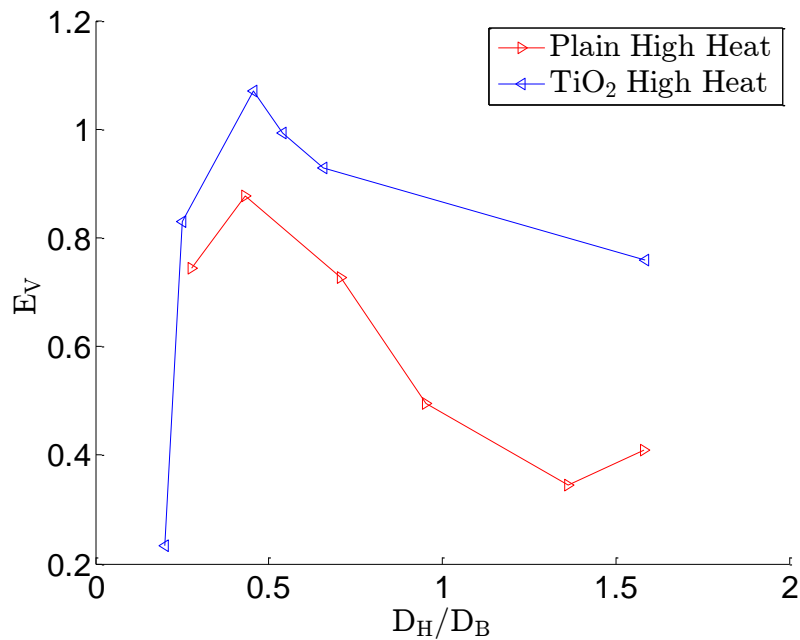


Figure 39 Relationship Between Dimensionless Heater Diameter and Vapor Effectiveness

Here, it can be seen that between 0.432 and 0.454 of a bubble diameter, the maximum benefit of the small heater diameter is seen. Additionally, the present study shows that wettable surfaces are more effective at producing vapor.

3.3 SINGLE-SITE BUBBLE GROWTH STUDY

The previous section outlines the effects of varying heater diameter on vapor effectiveness and attributes the behaviors to changes in microlayer heat transfer. The microlayer is the main path through which heat flows in order to produce vapor. As the microlayer grows over a heated region and subsequently recedes, leaving it dry, the vapor production, too, should change. This

section outlines the dimensionless growth rates of several bubbles and their relationship to heater diameter.

The technique employed to evaluate the microlayer first measures the instantaneous bubble volume as well as the instantaneous bubble base diameter for only a single bubble, and is quantified through image analysis from high speed camera data taken at 10,000 frames per second. Due to the wide variability in overall shape of the bubble during its growth, the volume is calculated as a stack of discs with a thickness of one pixel. The base diameter is simply the diameter of the disc closest to the solid substrate. These parameters are measured at each time step and a time history of bubble volume and base diameter is generated. The base diameter is assumed to be the same as the outer microlayer diameter. However, the dry spot diameter is not measured and must be taken from other literature.

The 2015 study by Jung and Kim [39] characterizes the microlayer geometry and shows the time history of the dry spot diameter and the outer diameter with respect to a dimensionless time. The dry spot consumes the microlayer by 65-70% of the growth time. Prior to that time, the dry spot diameter grows in a linear fashion from the bubble incipience with a dry spot diameter of zero. This behavior is very simple to simulate in the results of the present study as shown in Figure 40. The dry spot behavior is approximated by first identifying the time at which the dry spot occupies the entire microlayer. Based on Jung and Kim's [39] results, this time is assumed to be 0.7 of the departure time. The diameter at this instant is the maximum dry spot diameter and the diameters of each case are normalized by it. After 70% of the departure time, the dry spot diameter is the base diameter, so there is no calculation needed to determine the dry spot diameter. From 0-70% of the departure time, the dry spot is assumed to grow linearly from zero to 1. These steps are a concise approximation for dry spot growth.

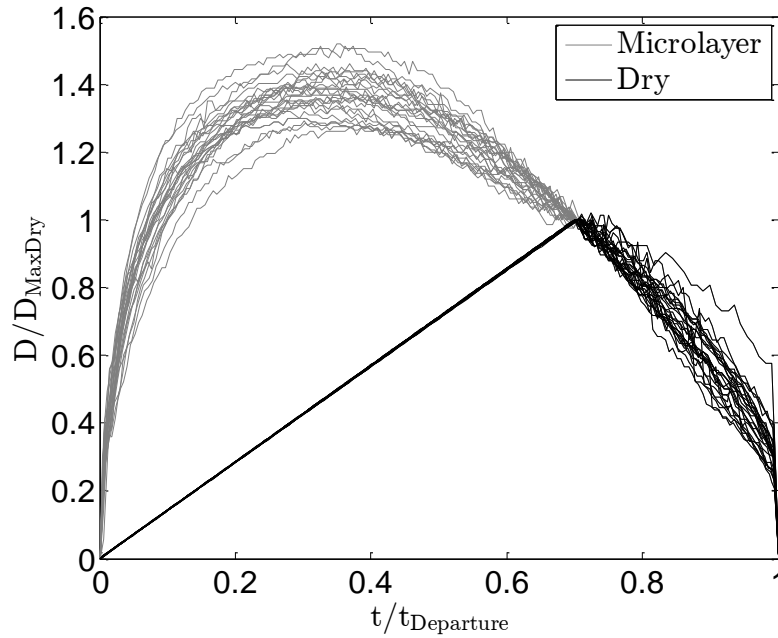


Figure 40 Normalized Growth of Bubble Base Diameter and Empirical Approximation of Dry Spot Diameter With Respect to Time

The ideal condition for maximizing vapor production would be complete coverage of the heated surface with the microlayer during peak heat transfer or for the entire duration. However, due to the presence of the dry spot, full microlayer coverage of the heater is impractical. Comparing the percentage of microlayer coverage of the heater area to the bubble growth rate at the corresponding time reveals the favorability of the microlayer condition at critical vapor production intervals. Therefore, a parameter representing the percent of heater area that is favorable for vapor generation is needed. The ratio of vapor generating heater area, R_{vga} , is introduced. Equation (11) defines the ratio of vapor generating area as the area of vapor generation divided by the heated area. If the bubble base diameter is smaller than the heater diameter, the area of vapor generation is the bubble base area minus the dry spot area. If the bubble base diameter is larger than the heater area, the area of vapor generation is the heater area

minus the dry spot area. For very small heater diameters, the value of the ratio of vapor generating heater area may become negative. In those cases, the ratio is set to zero.

$$R_{vga} = \frac{\min(A_{Base}, A_H) - A_{Dry}}{A_H} \quad (11)$$

In this comparison, dimensionless vapor generation rate is calculated using a forward difference time derivative of volume and subsequent spline smoothing to reduce noise from the numerical derivative. This smoothing is only used for better visualization and not for any calculations. Figure 41 through Figure 44 demonstrate that the larger heaters are never fully covered by the microlayer due to the microlayer never growing to the full size of the heater. Conversely, Figure 46 through Figure 48 show that smaller heaters, while more easily covered by the microlayer outer diameter, are quickly bare due to the growth of the dry spot. The best compromises for microlayer coverage are seen in Figure 44, Figure 45 and Figure 46. It is important to note that once the dry spot consumes the microlayer, no credit is given to the small area coverage offered by the triple contact line.

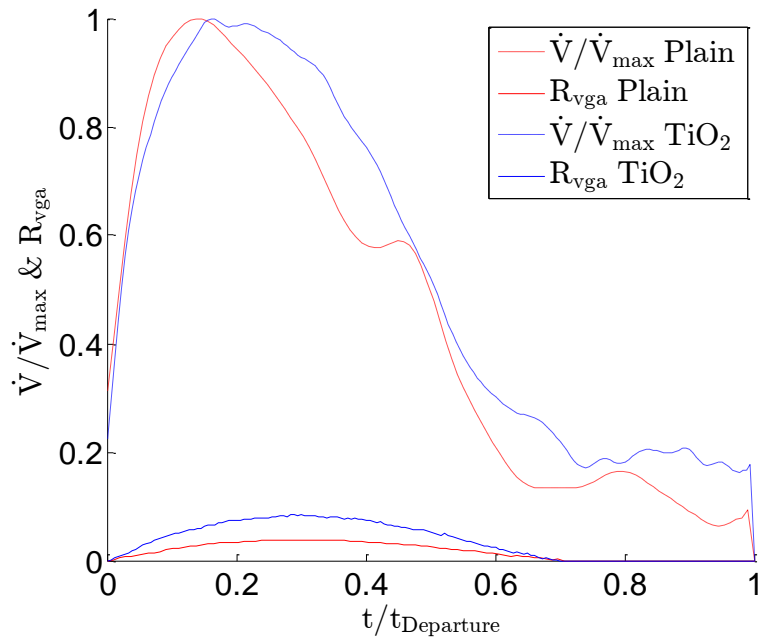


Figure 41 Percent of Microlayer that is Heated and Wetted And Dimensionless Bubble Growth Rate with Respect to Normalized Time for 9.52mm Heater

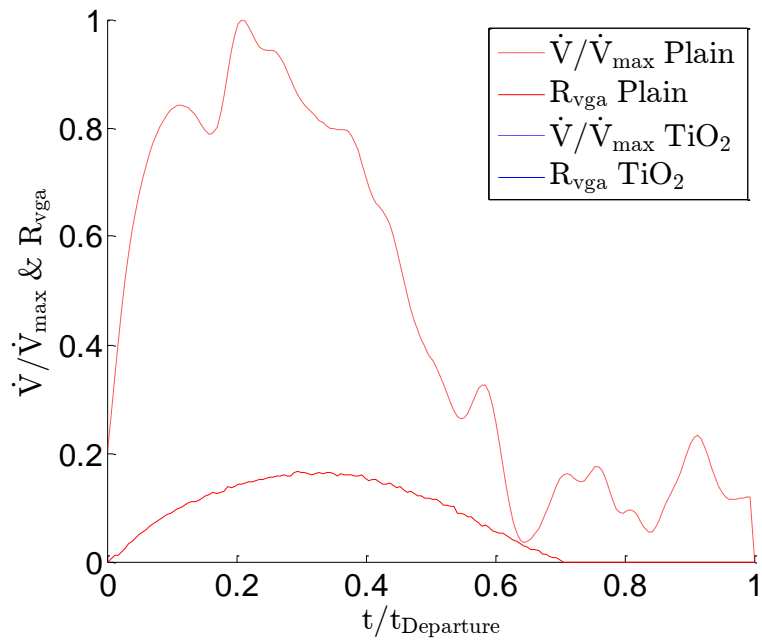


Figure 42 Percent of Microlayer that is Heated and Wetted And Dimensionless Bubble Growth Rate with Respect to Normalized Time for 7.94mm Heater

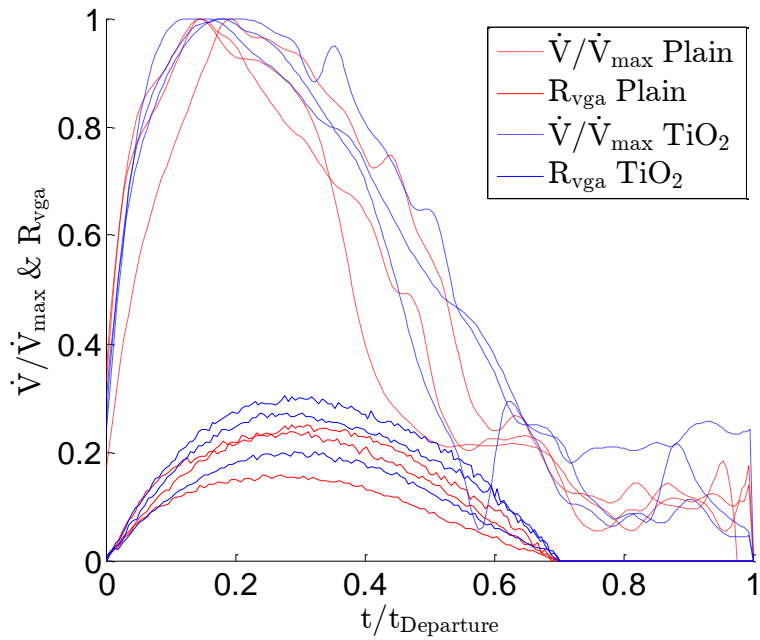


Figure 43 Percent of Microlayer that is Heated and Wetted And Dimensionless Bubble Growth Rate with Respect to Normalized Time for 6.35mm Heater

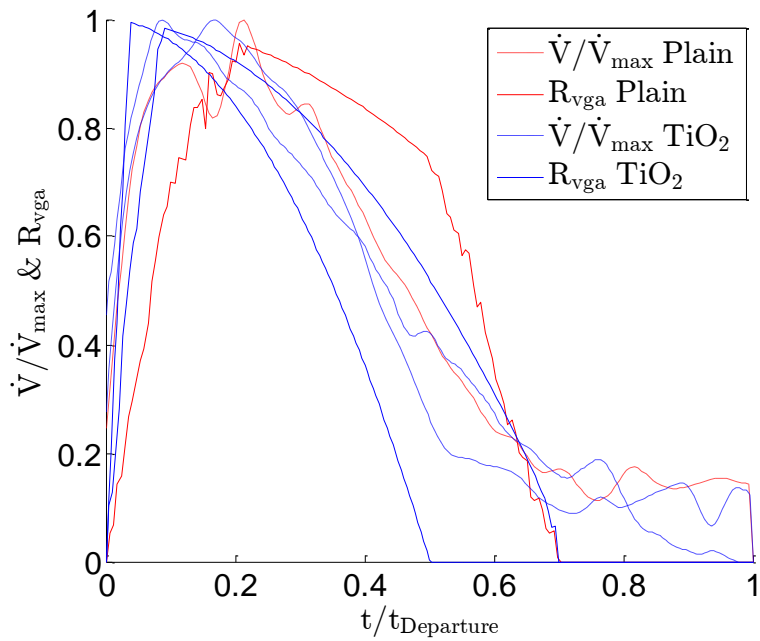


Figure 44 Percent of Microlayer that is Heated and Wetted And Dimensionless Bubble Growth Rate with Respect to Normalized Time for 3.18mm Heater

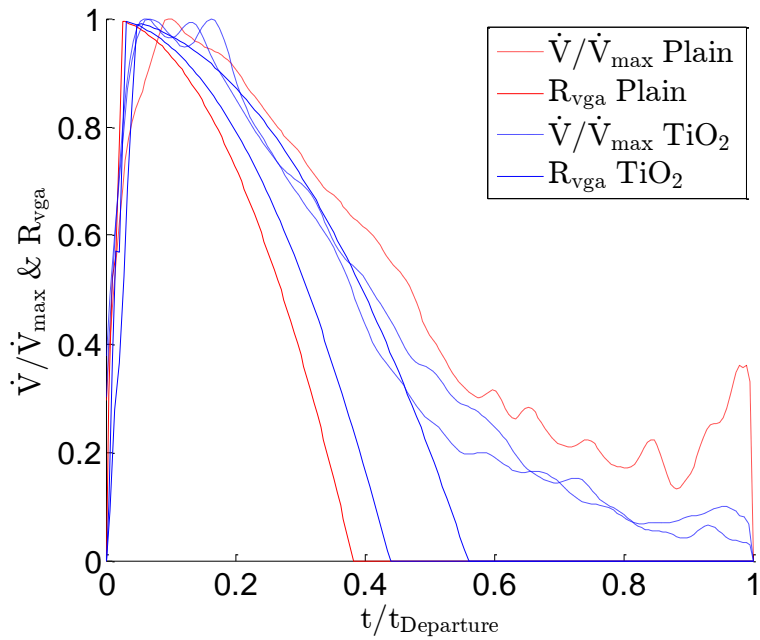


Figure 45 Percent of Microlayer that is Heated and Wetted And Dimensionless Bubble Growth Rate with Respect to Normalized Time for 2.00mm Heater

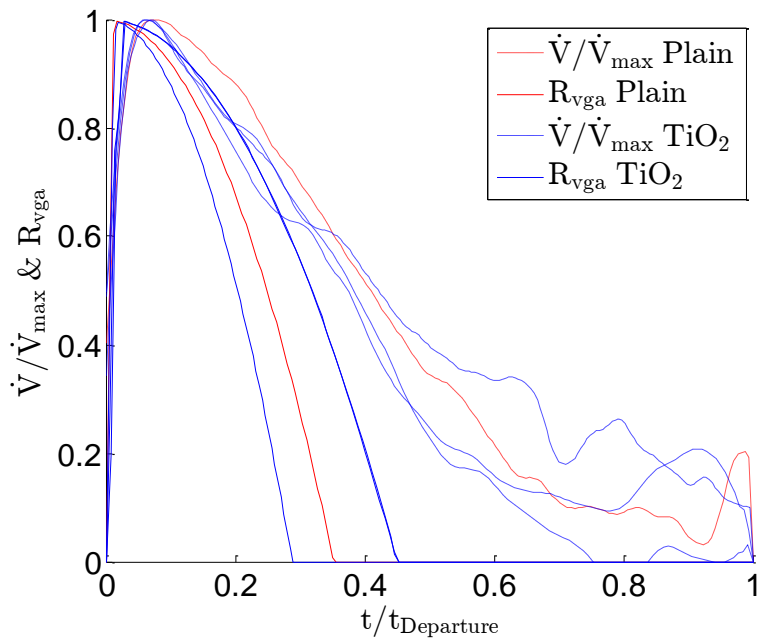


Figure 46 Percent of Microlayer that is Heated and Wetted And Dimensionless Bubble Growth Rate with Respect to Normalized Time for 1.50mm Heater

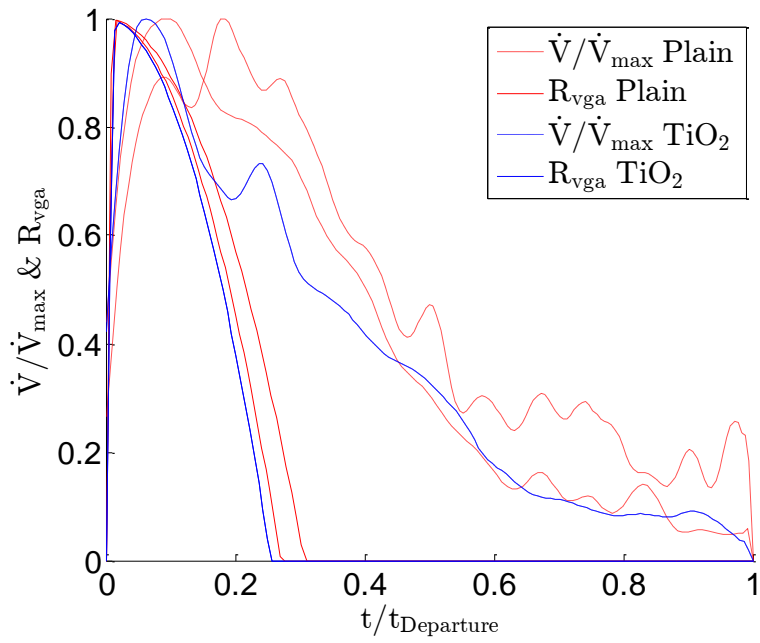


Figure 47 Percent of Microlayer that is Heated and Wetted And Dimensionless Bubble Growth Rate with Respect to Normalized Time for 1.00mm Heater

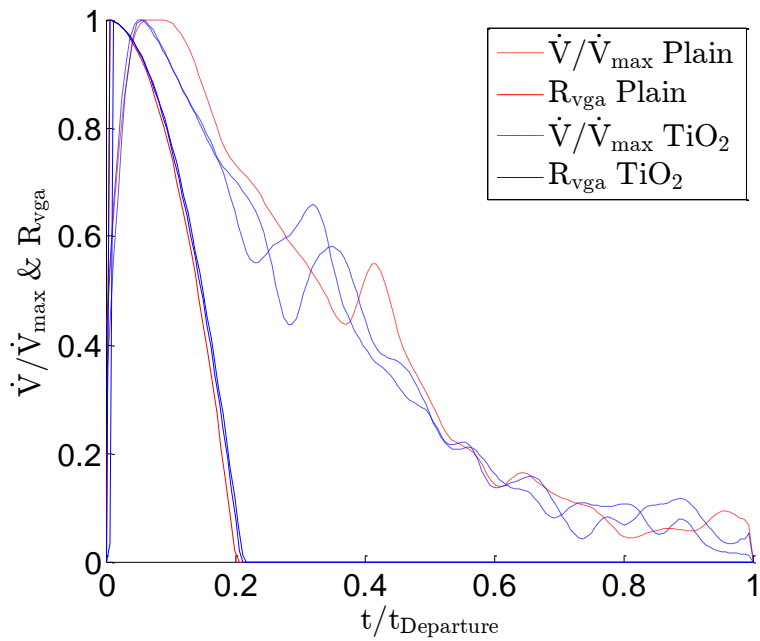


Figure 48 Percent of Microlayer that is Heated and Wetted And Dimensionless Bubble Growth Rate with Respect to Normalized Time for 0.80mm Heater

These figures visually illustrate the alignment of microlayer coverage and vapor production. A more condensed evaluation of this metric is the time integral of the product of the two curves. The volume rate is re-normalized by the departure volume such that the integral with respect to the full time duration results in a volume of unity. Therefore, if continuous microlayer coverage of 100% was used for any of the volume rate curves, unity would result. Equation (12) shows the integral form of the microlayer coverage growth parameter, λ .

$$\lambda = \frac{1}{V} \int_0^1 \dot{V}(t) R_{vga}(t) dt \quad (12)$$

The results agree with earlier observations that larger heaters are not adequately covered by the microlayer while smaller heaters dry out too quickly. Figure 49 shows that the two smallest and three largest heaters do not have microlayer coverage that coincides well with vapor generation. Nondimensionalizing the heater diameter with respect to the bubble departure diameter in the same fashion as the single site bubble sequence study yields a trend similar to that in Figure 37. The peak coincidence of microlayer coverage and vapor generation occurs between 0.37-0.57 dimensionless heater diameters. Within this range the heaters are experiencing the best microlayer conditions for heat transfer. Outside this range, a greater portion of vapor is being generated while dry or while wetted with bulk, non-microlayer fluid. There is a peak in performance from the single-site bubble sequence study that agrees with the peak in coincidence of microlayer coverage and vapor generation. This corroborates the suggestion that the variability in heater performance was due to microlayer contribution. Furthermore, it suggests that the reduction in performance of the small heaters was due to drying of the heater surface while that of the larger heaters was due to heating of the bulk fluid because of inadequate coverage by the microlayer.

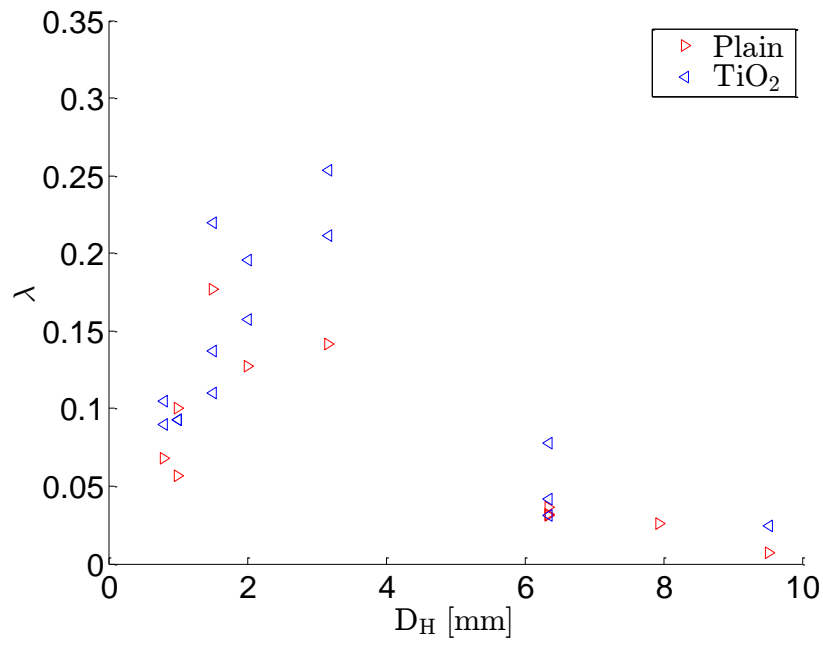


Figure 49 Heater Diameter Compared to Coincidence of Heater Coverage by Microlayer

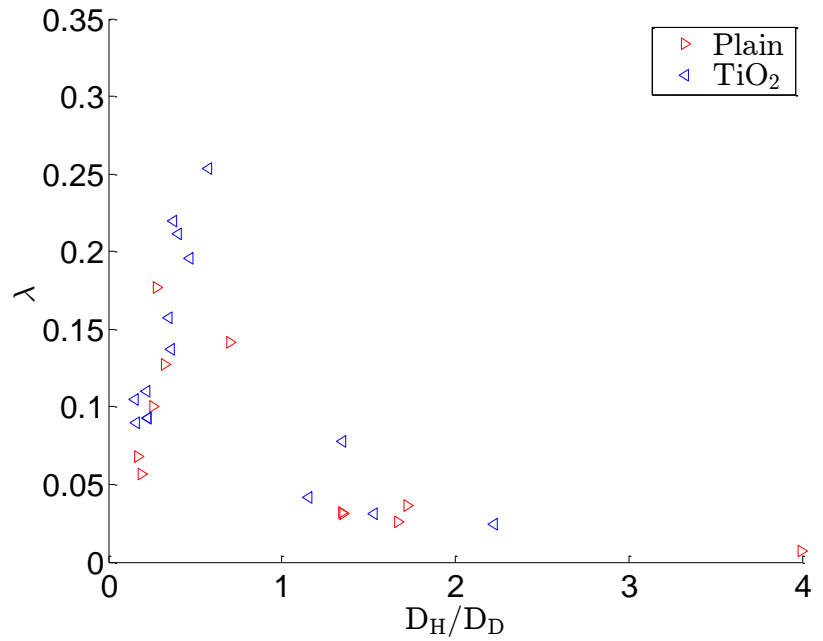


Figure 50 Dimensionless Heater Diameter Compared to Coincidence of Heater Coverage by Microlayer

Microlayer coverage of the heater can be influenced by the heater geometry with respect to the bubble geometry. However, whether the heater geometry actually influences the microlayer development is unknown. One parameter that likely affects the microlayer growth and subsequent dryout is the wettability. The microlayer geometry cannot be completely measured using the instruments from this study. However, it is possible to compare the microlayer performance of the two surfaces. In general, the coated surfaces appear to have better microlayer coverage than the uncoated surfaces. In a direct comparison, the average of the coated cases is compared to the average of the uncoated cases for each heater diameter. Figure 51 shows this relationship. In every case but the 1.5mm heater diameter, the coated case outperformed the uncoated case. The average ratio of the λ values is 1.66 in favor of the coated cases.

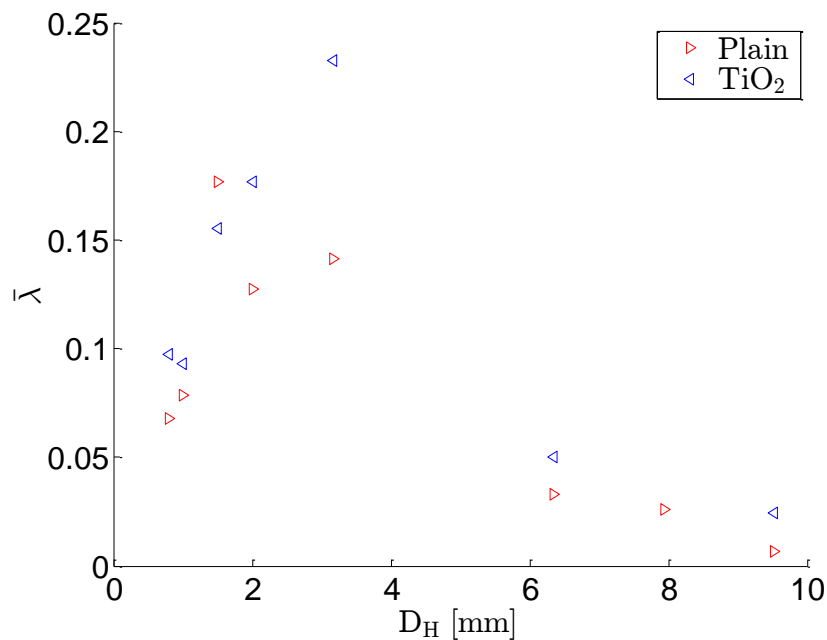


Figure 51 Heater Diameter Compared to Average Coincidence of Heater Coverage by Microlayer

It is intuitive that a more wettable surface would better cover the microlayer. The improvement of the microlayer coverage afforded by the more wettable surface is a possible explanation for the slightly better performance of the coated surface in the single site bubble sequence study. However the dry spot diameter was not directly measured. Therefore, a separate study of the microlayer geometries of varying wettability surfaces is needed.

4.0 FUTURE WORK

The main focus of the present work is characterizing vapor effectiveness and identifying factors contributing to this parameter in both single and double nucleation sites. Vapor effectiveness, by itself, is not a useful parameter for practical purposes. However it does reveal the utilization of energy in the microlayer. With uniform heating, it has been shown that proximity between neighboring sites only reduces overall vapor effectiveness. Hydrodynamic parameters such as bubble departure width and departure velocity reduced their positive influence with the presence of adjacent sites. However, with constricted heaters, the mechanisms are fundamentally altered; namely the thermal boundary layer. The behavior of two constricted heaters in close proximity is not captured in this study, but is worthy of further investigations. In that scenario, with the absence of a thermal boundary layer the two sites will no longer be competing over superheated liquid energy. Thus, there may be a less detrimental effect on vapor effectiveness resulting from reduced spacing compared with a surface with an appreciable thermal boundary layer. Once the effect of the spacing of constricted heaters is better understood, their practical use can be explored.

In a 2013 study, Betz et al [21] studied biphilic and superbiphilic patterns with the majority of the surface area favorable for high heat flux performance while small, regular spots of the surface are optimized for low heat flux performance. The heat transfer coefficients of these surfaces were reported to be 3 times higher than the best previous surface. These surfaces

entirely rely upon the effects of surface tension to increase heat transfer performance. The present study takes advantage of knowledge of heat transfer within the substrate to generate the highest number of bubbles with the smallest supply of heat to the surface.

Similarly, a more practical surface should be designed to employ the knowledge of the present study and the proposed study above. Such a surface would allow channels of heat to flow into carefully spaced, isolated nucleation sites at lower heat fluxes to drive efficient bubbling while permitting nucleation everywhere under high heat fluxes. This task could be accomplished by an array of wide conical cavities with nucleation sites at the lowest points. Alternatively, a matrix of insulating material with vertical channels of conductive material would allow nucleation sites to bubble without being suppressed by neighboring sites. Figure 52 shows a cartoon of these proposed engineering surfaces.

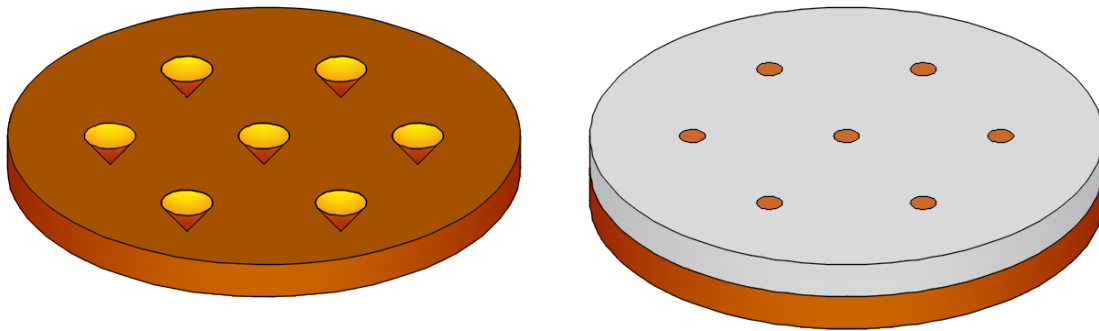


Figure 52 Suggested Configurations for Practical Engineered Heater Surfaces

This hypothetical surface might have effective bubbling at low heat flux, while higher heat flux may not be as effective. If a successful implementation of such a surface were achieved, it could have greater longevity in an industrial environment than a coated surface.

5.0 CONCLUSION

The present study demonstrates and explains new bubbling behaviors as well as adds perspective on behaviors previously observed. Table 4 outlines the contributions of the present work. The apparatus used to observe these behaviors is relatively simple, but utilizes novel surface treatments and heater configurations to control nucleation. The multi-site study shows that the promotive hydrodynamic effects are weakened with the presence of additional nucleation sites. A mechanistic explanation is suggested which proposes that superheated areas above nucleation sites are the object of competition between neighboring sites. This explanation supports the observation that greater spacing improves vapor effectiveness. The single site study further supports the suggested explanation by showing that hydrodynamic effects do not influence vapor effectiveness with constricted heaters and subsequently reduced or eliminated thermal boundary layers. The single site also demonstrated that less heat is required for the onset of nucleate boiling with reduced heater area. Smaller heaters are shown to be more effective at producing vapor as long as they are above a sharp lower limit. Therefore, an optimum heater diameter is suggested. The mechanism permitting this optimization is microlayer coverage of the heated area during high growth rate. Surfaces that are more wettable are also demonstrated to produce vapor more effectively which is likely caused by better coverage of the heated area caused by the surface's additional affinity for water.

Table 4 Contributions of Present Study

<ul style="list-style-type: none"> • Demonstrate the ability to create nucleation sites using high contrast wettability pattern
<ul style="list-style-type: none"> • Identify direct relationship between site spacing and vapor effectiveness
<ul style="list-style-type: none"> • Demonstrate strong relationship between hydrodynamic factors and vapor effectiveness for single site. Demonstrate weaker Relationship for multi-site configuration. Propose explanation of displacement of superheated pocket.
<ul style="list-style-type: none"> • Show that vapor effectiveness is decoupled from hydrodynamic effects when heater area is restricted; supporting the suggestion that superheated liquid is the object of competition between nucleation sites.
<ul style="list-style-type: none"> • Demonstrate strong relationship between heater size and heat required for ONB
<ul style="list-style-type: none"> • Demonstrate inverse relationship between heater size and vapor effectiveness and identify lower limit of this behavior
<ul style="list-style-type: none"> • Quantify optimum heater diameter. Heater diameters of approximately 1.25mm or 0.443 bubble diameters have the highest vapor effectiveness.
<ul style="list-style-type: none"> • Demonstrate that wettable surface produces vapor more effectively than non wettable surface
<ul style="list-style-type: none"> • Estimate microlayer geometry using current experimental results to determine microlayer outside diameter and previous studies to determine dry spot diameter
<ul style="list-style-type: none"> • Develop a metric that evaluates microlayer coverage of the heated area and compares to coincident bubble growth rates
<ul style="list-style-type: none"> • Demonstrate that the optimum vapor effectiveness and peak coincidence of microlayer coverage and vapor generation occur at nearly identical dimensionless heater diameters. Conclude that timely microlayer coverage is responsible for maximum vapor effectiveness.
<ul style="list-style-type: none"> • Recommend a multi-site constricted heater study to confirm present multisite assertions. Propose the manufacture and testing of an engineering surface that maximizes vapor effectiveness in a multi-site array.

Finally, a recommendation is made for a preliminary multi-site study with optimized heater diameters followed by a study of a practical engineering surface. Both of these studies would take advantage of conclusions made in the present study but have the ultimate aim of creating a surface that could be useful for vapor production or multiphase cooling.

APPENDIX A

DERIVATION OF PIN FIN EQUATION WITH VARIABILITY THERMAL CONDUCTIVITY

The following text outlines the derivation for a fin with variable thermal conductivity and constant circular cross section. This derivation follows a similar form as found in Incropera & Dewitt's Fundamentals of Heat and Mass Transfer [41] pin fin derivation. Conservation of energy begins the derivation with accompanying Figure 53.

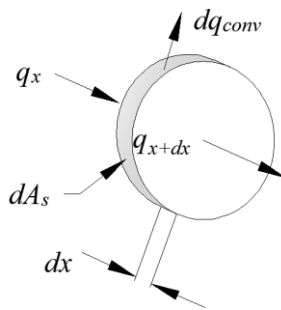


Figure 53 Diagram of differential element

In Equation (13) it can be seen that to balance the difference in the flux at the inlet and outlet of the differential element, the differential dq_{conv} is added. Equation (14) reiterates Fourier's law of heat conduction and Equation (15) defines q_{x+dx} in differential terms.

$$q_x = q_{x+dx} + dq_{conv} \quad (13)$$

$$q_x = -kA_c \frac{dT}{dx} \quad (14)$$

$$q_{x+dx} = q_x + \frac{dq_x}{dx} dx \quad (15)$$

Equation (16) substitutes the known expressions into Equation (15) and employs the chain rule for dq_x/dx . Equation (17) defines the energy lost along the perimeter with an adaptation of Newton's law of cooling.

$$q_{x+dx} = -kA_c \frac{dT}{dx} - A_c \frac{dk}{dx} \frac{dT}{dx} dx + -A_c k \frac{d^2T}{dx^2} dx \quad (16)$$

$$dq_{conv} = hdA_s(T - T_\infty) \quad (17)$$

Equation (18) returns to the conservation of energy equation and cancels terms.

$$k \frac{d^2T}{dx^2} + \frac{dk}{dx} \frac{dT}{dx} - \frac{h}{A_c} \frac{dA_s}{dx} (T - T_\infty) = 0 \quad (18)$$

In Equation (19), the derivative of surface area with respect to length is simply the perimeter for fins of constant cross section.

$$\frac{dA_s}{dx} = P \quad (19)$$

Equation (20) employs the chain rule and Equation (19) in the conservation of energy equation.

$$k \frac{d^2 T}{dx^2} + \frac{dk}{dT} \frac{dT}{dx} \frac{dT}{dx} - \frac{hP}{A_c} (T - T_\infty) = 0 \quad (20)$$

$$\frac{d^2 T}{dx^2} + \frac{1}{k} \frac{dk}{dT} \left(\frac{dT}{dx} \right)^2 - \frac{4h}{kD} (T - T_\infty) = 0 \quad (21)$$

Equation (21) collects terms and applies conditions for constant circular cross section. This concludes the derivation of the fin equation for variable conductivity with constant circular cross section.

APPENDIX B

SURFACE CHARACTERIZATION OF ALD AND PLAIN SURFACES

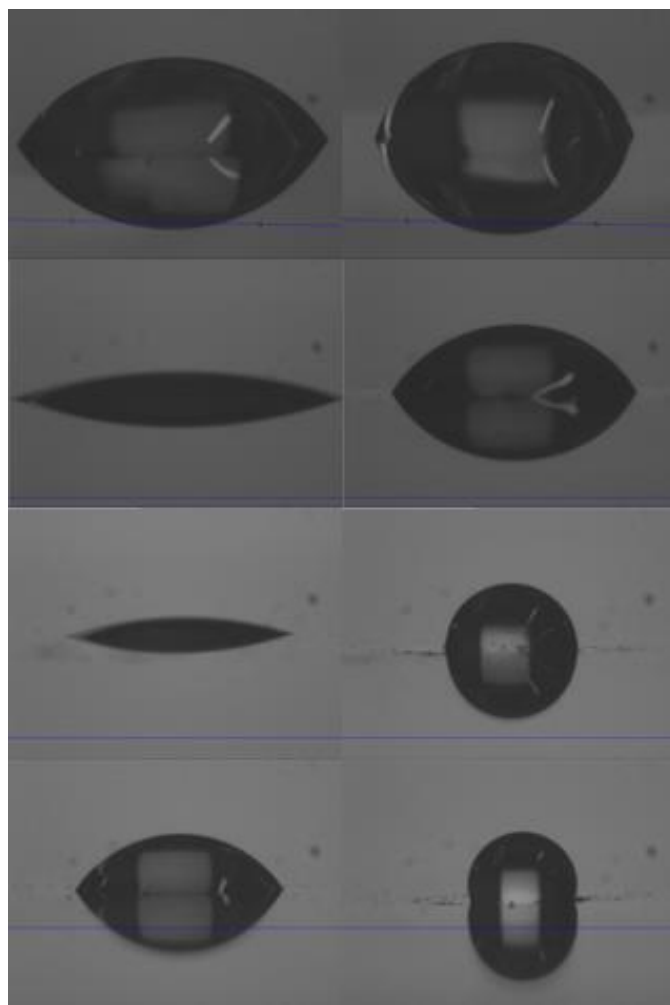


Figure 54 Contact Angles Surfaces 1 through 4. Left Column Hydrophilic Right Column Hydrophobic

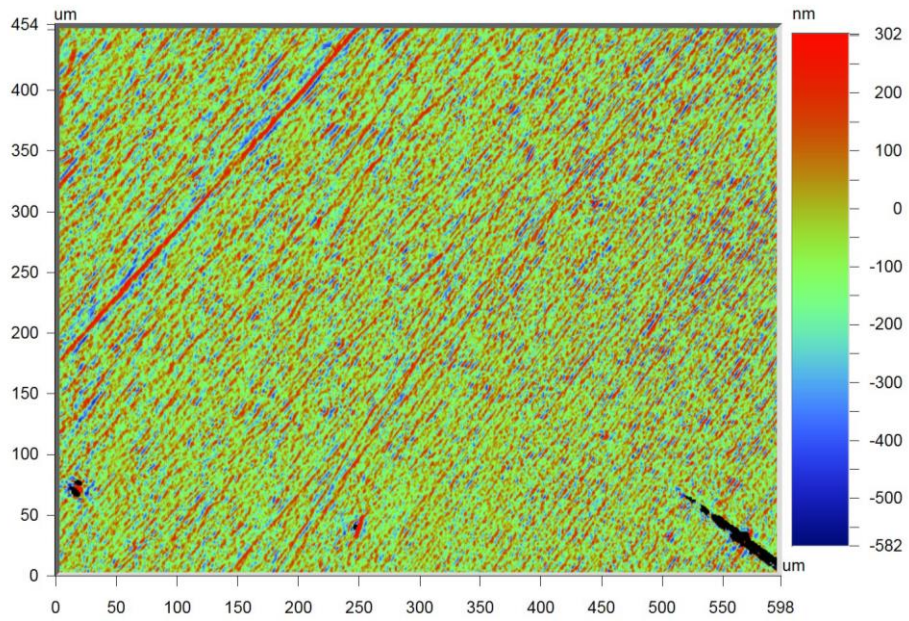


Figure 55 Surface 1 Hydrophobic Region Ra 28.21nm

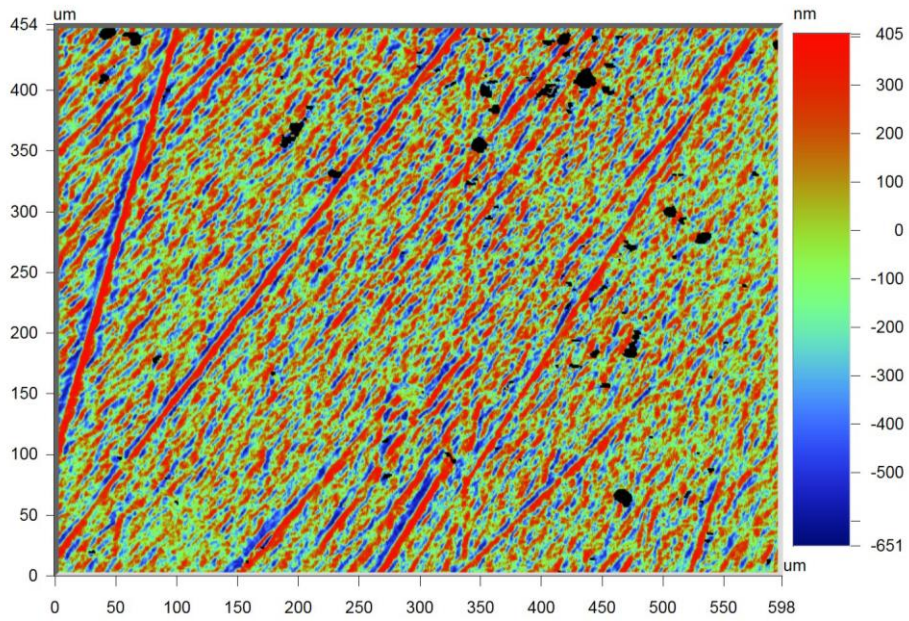


Figure 56 Surface 2 Hydrophobic Region Ra 72.67nm

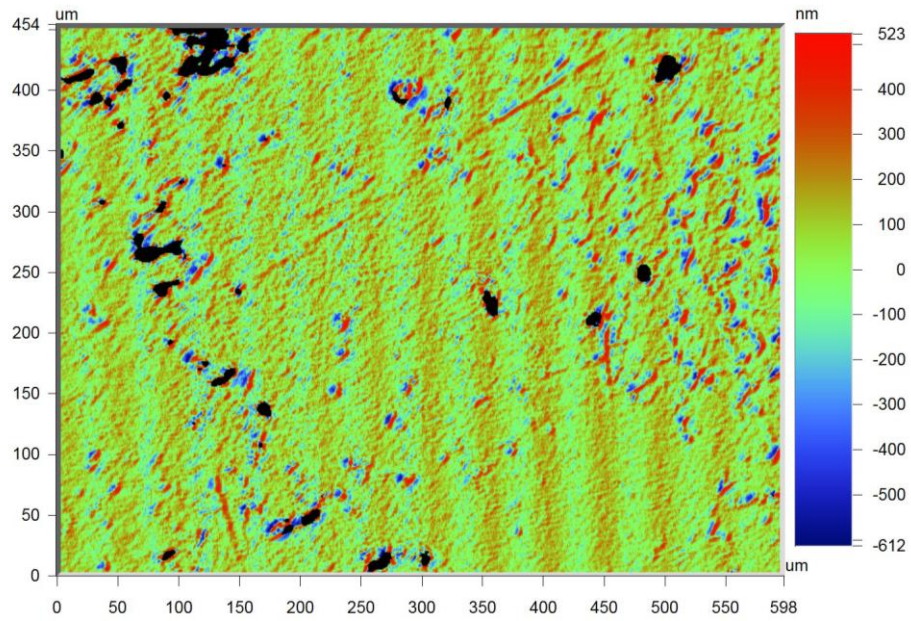


Figure 57 Surface 3 Hydrophobic Region Ra 58.33nm

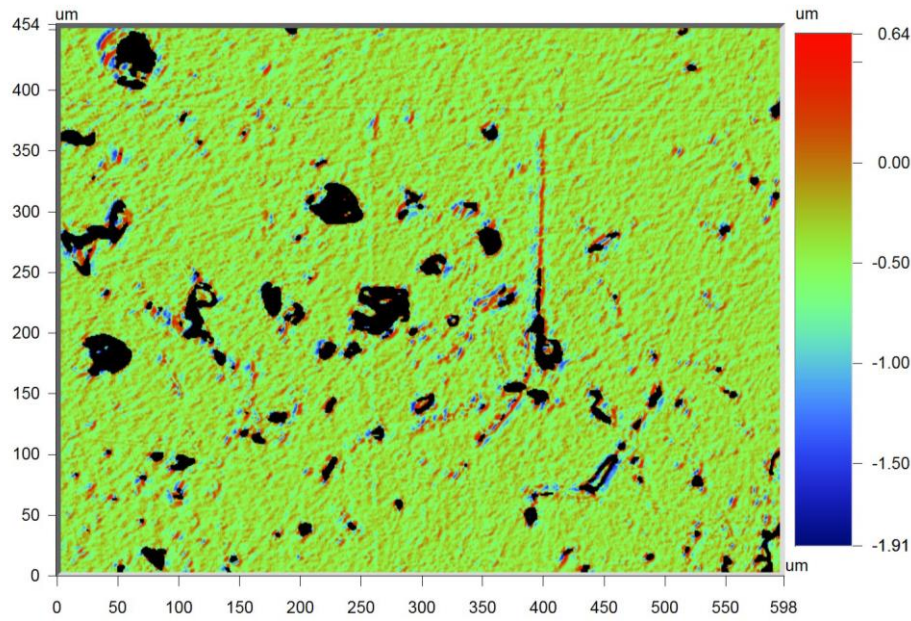


Figure 58 Surface 4 Hydrophobic Region Ra 34.46nm

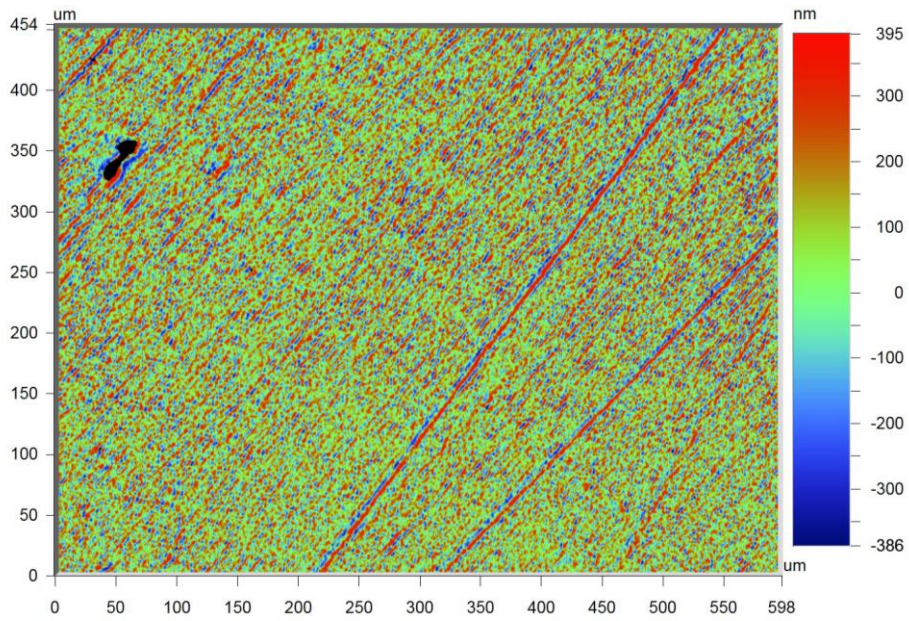


Figure 59 Surface 1 Hydrophilic Region Ra 23.73nm

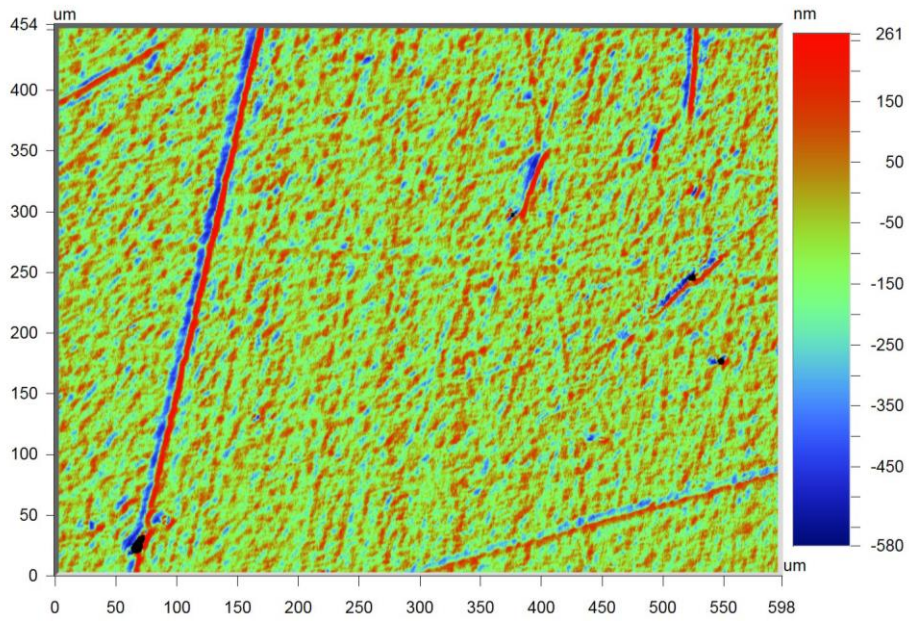


Figure 60 Surface 2 Hydrophilic Region Ra 31.86nm

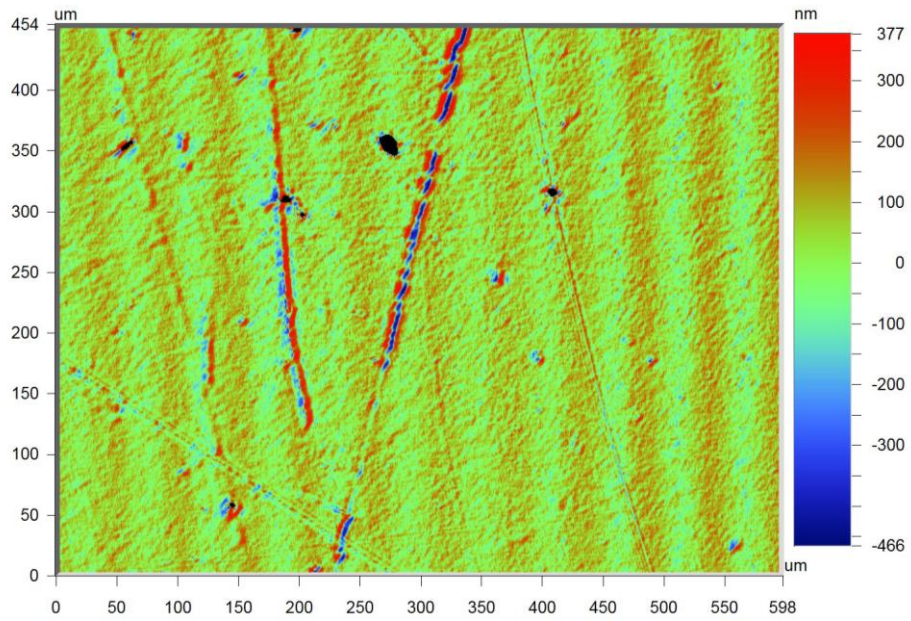


Figure 61 Surface 3 Hydrophilic Region Ra 29.99nm

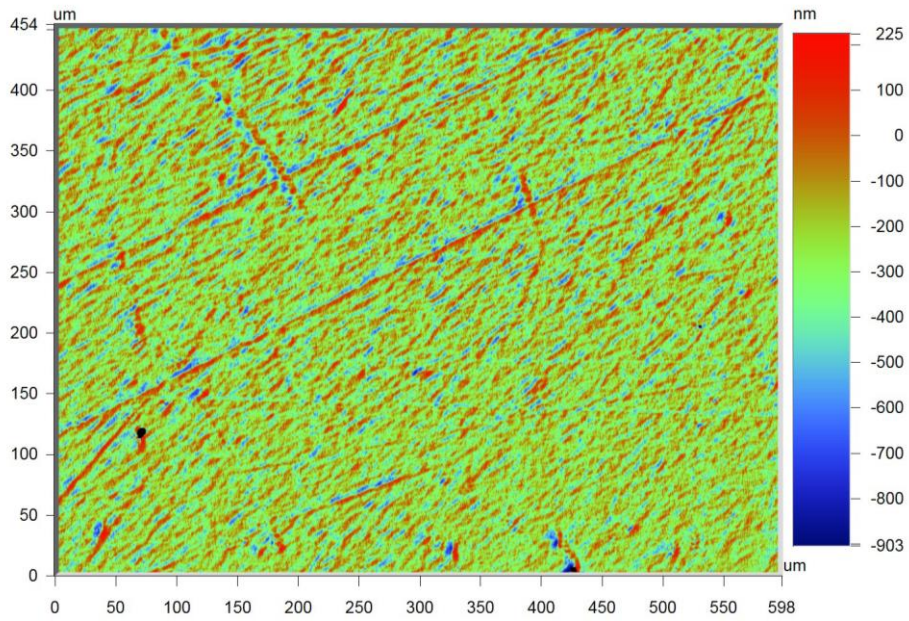


Figure 62 Surface 4 Hydrophilic Region Ra 33.86nm

APPENDIX C

EVALUATION OF SUITABILITY OF DIMENSIONLESS SPACING FOR VAPOR EFFECTIVENESS STUDIES

The present study does not employ the dimensionless spacing, S/D_B like other similar studies. Indeed, one of the main purposes of normalizing the site spacing with respect to bubble diameter is to account for these hydrodynamic, thermal and coalescence factors with a proportionally scaled dimensionless group, S/D_B . However, while this dimensionless group is useful for the departure frequency study, it is not appropriate for the vapor effectiveness study. A comparison of Figure 63 and Figure 64 demonstrates why dimensionless spacing was not used for this study. Figure 63 illustrates a series of cases observed with two nucleation sites and compares the departure frequency to the dimensionless site spacing. However, there is a single data point in that series where the site spacing was smaller but still has a similar dimensionless spacing to the rest of the group. Indeed, for the departure frequency study, it does fit into the group. However, Figure 64 plots the same cases against vapor effectiveness and the single data point becomes an outlier different by an approximate factor of seven. This is because the dimensionless site spacing is not an appropriate dimensionless group for vapor effectiveness prediction. This finding supports the decision to abandon the dimensionless site spacing for the purposes of the vapor effectiveness study.

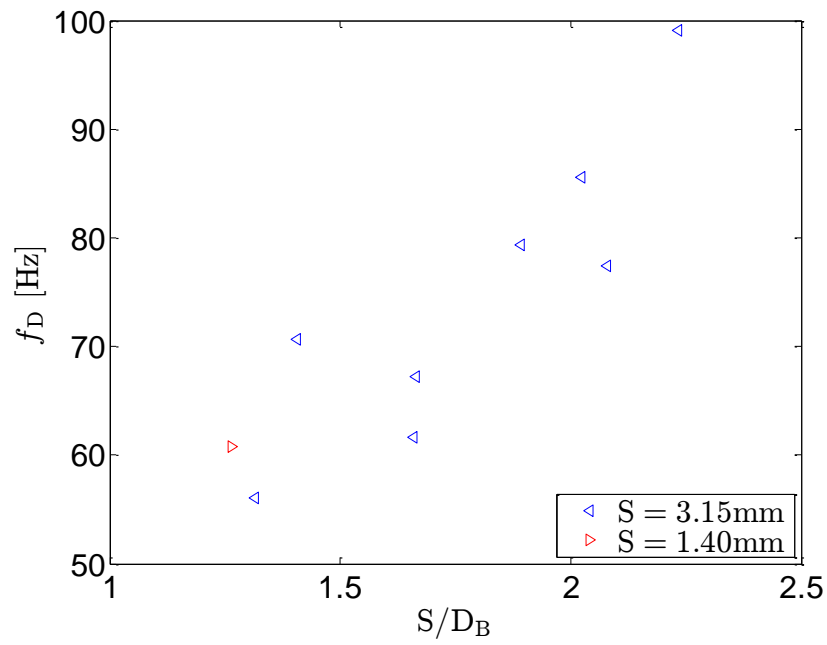


Figure 63 Comparison of Dimensionless Site Spacing and Departure Frequency for Double Site Configurations

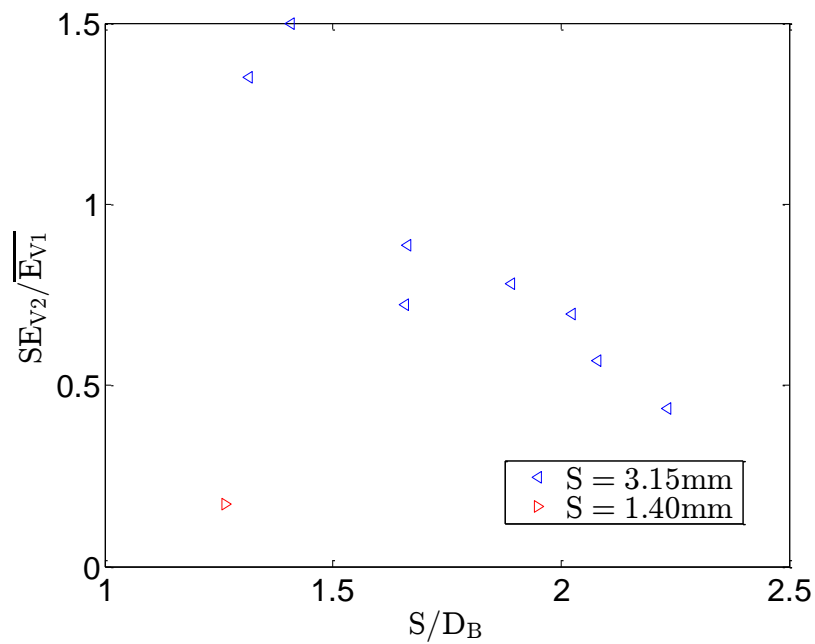


Figure 64 Comparison of Dimensionless Site Spacing and Superficial Vapor Effectiveness Ratio for Double Site Configurations

BIBLIOGRAPHY

- [1] Dhir, V. K. "Boiling heat transfer." *Annual review of fluid mechanics* 30.1 (1998): 365-401.
- [2] Shoji, Masahiro, and Yuto Takagi. "Bubbling features from a single artificial cavity." *International journal of heat and mass transfer* 44.14 (2001): 2763-2776.
- [3] Siedel, S., S. Cioulachtjian, and J. Bonjour. "Experimental analysis of bubble growth, departure and interactions during pool boiling on artificial nucleation sites." *Experimental Thermal and Fluid Science* 32.8 (2008): 1504-1511.
- [4] Phan, Hai Trieu, et al. "Surface wettability control by nanocoating: the effects on pool boiling heat transfer and nucleation mechanism." *International Journal of Heat and Mass Transfer* 52.23 (2009): 5459-5471.
- [5] Phan, Hai Trieu, et al. "A model to predict the effect of contact angle on the bubble departure diameter during heterogeneous boiling." *International Communications in Heat and Mass Transfer* 37.8 (2010): 964-969.
- [6] Nam, Youngsuk, et al. "Single bubble dynamics on a superhydrophilic surface with artificial nucleation sites." *International Journal of Heat and Mass Transfer* 54.7 (2011): 1572-1577.
- [7] Yabuki, Tomohide, Takuya Hamaguchi, and Osamu Nakabeppu. "Interferometric measurement of the liquid-phase temperature field around an isolated boiling bubble." *Journal of Thermal Science and Technology* 7.3 (2012): 463-474.
- [8] Yabuki, Tomohide, and Osamu Nakabeppu. "Heat transfer mechanisms in isolated bubble boiling of water observed with MEMS sensor." *International Journal of Heat and Mass Transfer* 76 (2014): 286-297.
- [9] Zhang, Lei, and Masahiro Shoji. "Nucleation site interaction in pool boiling on the artificial surface." *International Journal of Heat and Mass Transfer* 46.3 (2003): 513-522.
- [10] Chatpun, Surapong, Makoto Watanabe, and Masahiro Shoji. "Nucleation site interaction in pool nucleate boiling on a heated surface with triple artificial cavities." *International journal of heat and mass transfer* 47.14 (2004): 3583-3587.

- [11] Chekanov, V. V. "Interaction of centers in nucleate boiling." *High Temp.(USSR)(Engl. Transl.);(United States)* 15.1 (1977).
- [12] Calka, Andrej, and Ross L. Judd. "Some aspects of the interaction among nucleation sites during saturated nucleate boiling." *International journal of heat and mass transfer* 28.12 (1985): 2331-2342.
- [13] Nimkar, Nitesh D., Sushil H. Bhavnani, and Richard C. Jaeger. "Effect of nucleation site spacing on the pool boiling characteristics of a structured surface." *International journal of heat and mass transfer* 49.17 (2006): 2829-2839.
- [14] Golobič, Iztok, and Henrik Gjerkeš. "Interactions between laser-activated nucleation sites in pool boiling." *International journal of heat and mass transfer* 44.1 (2001): 143-153.
- [15] Bonjour, Jocelyn, Marc Clausse, and Monique Lallemand. "Experimental study of the coalescence phenomenon during nucleate pool boiling." *Experimental Thermal and Fluid Science* 20.3 (2000): 180-187.
- [16] Chen, Tailian, and J. N. Chung. "Coalescence of bubbles in nucleate boiling on microheaters." *International Journal of Heat and Mass Transfer* 45.11 (2002): 2329-2341.
- [17] Chen, Tailian, and J. N. Chung. "Heat-transfer effects of coalescence of bubbles from various site distributions." *Proceedings of the Royal Society of London A: Mathematical, Physical and Engineering Sciences*. Vol. 459. No. 2038. The Royal Society, 2003.
- [18] von Hardenberg, Jost, et al. "Identification of nucleation site interactions." *International journal of heat and fluid flow* 25.2 (2004): 298-304.
- [19] Hutter, C., et al. "Nucleation site interaction between artificial cavities during nucleate pool boiling on silicon with integrated micro-heater and temperature micro-sensors." *International Journal of Heat and Mass Transfer* 55.11 (2012): 2769-2778.
- [20] Jingliang, Bi, Lin Xipeng, and David M. Christopher. "Effects of bubble coalescence dynamics on heat flux distributions under bubbles." *AIChE Journal* 59.5 (2013): 1735-1745.
- [21] Betz, Amy Rachel, James Jenkins, and Daniel Attinger. "Boiling heat transfer on superhydrophilic, superhydrophobic, and superbiphilic surfaces." *International Journal of Heat and Mass Transfer* 57.2 (2013): 733-741.
- [22] Betz, Amy Rachel, et al. "Do surfaces with mixed hydrophilic and hydrophobic areas enhance pool boiling?." *Applied Physics Letters* 97.14 (2010): 141909.
- [23] Moore, Franklin D., and Russell B. Mesler. "The measurement of rapid surface temperature fluctuations during nucleate boiling of water." *AIChE Journal* 7.4 (1961): 620-624.

- [24] Jawurek, H. H. "Simultaneous determination of microlayer geometry and bubble growth in nucleate boiling." *International Journal of Heat and Mass Transfer* 12.8 (1969): 843IN1847-846IN2848.
- [25] Koffman, Larry Douglas. *I. Experimental observations of the microlayer in vapor bubble growth on a heated solid. II. An investigation of the theory of evaporation and condensation*. Diss. California Institute of Technology, 1980.
- [26] Cooper, M. G., and A. J. P. Lloyd. "The microlayer in nucleate pool boiling." *International Journal of Heat and Mass Transfer* 12.8 (1969): 895-913.
- [27] Myers, Jerry G., et al. "Time and space resolved wall temperature and heat flux measurements during nucleate boiling with constant heat flux boundary conditions." *International Journal of Heat and Mass Transfer* 48.12 (2005): 2429-2442.
- [28] Das, A. K., P. K. Das, and P. Saha. "Heat transfer during pool boiling based on evaporation from micro and macrolayer." *International Journal of Heat and Mass Transfer* 49.19 (2006): 3487-3499.
- [29] Golobic, I., et al. "Experimental determination of transient wall temperature distributions close to growing vapor bubbles." *Heat and mass transfer* 45.7 (2009): 857-866.
- [30] Golobic, I., J. Petkovsek, and D. B. R. Kenning. "Bubble growth and horizontal coalescence in saturated pool boiling on a titanium foil, investigated by high-speed IR thermography." *International Journal of Heat and Mass Transfer* 55.4 (2012): 1385-1402.
- [31] Gao, Ming, et al. "An investigation of microlayer beneath nucleation bubble by laser interferometric method." *International Journal of Heat and Mass Transfer* 57.1 (2013): 183-189.
- [32] Utaka, Yoshio, et al. "Heat transfer characteristics based on microlayer structure in nucleate pool boiling for water and ethanol." *International Journal of Heat and Mass Transfer* 68 (2014): 479-488.
- [33] Gerardi, Craig, et al. "Study of bubble growth in water pool boiling through synchronized, infrared thermometry and high-speed video." *International Journal of Heat and Mass Transfer* 53.19 (2010): 4185-4192.
- [34] Kim, Hyungdae, and Jacopo Buongiorno. "Detection of liquid–vapor–solid triple contact line in two-phase heat transfer phenomena using high-speed infrared thermometry." *International Journal of Multiphase Flow* 37.2 (2011): 166-172.
- [35] Kim, Hyungdae, Youngjae Park, and Jacopo Buongiorno. "Measurement of wetted area fraction in subcooled pool boiling of water using infrared thermography." *Nuclear Engineering and Design* 264 (2013): 103-110.

- [36] Duan, X., et al. "Synchronized high-speed video, infrared thermometry, and particle image velocimetry data for validation of interface-tracking simulations of nucleate boiling phenomena." *Experimental Heat Transfer* 26.2-3 (2013): 169-197
- [37] Buongiorno, Jacopo, et al. "Micro-and nanoscale measurement methods for phase change heat transfer on planar and structured surfaces." *Nanoscale and Microscale Thermophysical Engineering* 18.3 (2014): 270-287.
- [38] Jung, Satbyoul, and Hyungdae Kim. "An experimental method to simultaneously measure the dynamics and heat transfer associated with a single bubble during nucleate boiling on a horizontal surface." *International Journal of Heat and Mass Transfer* 73 (2014): 365-375.
- [39] Jung, Satbyoul, and Hyungdae Kim. "An Experimental Study on Heat Transfer Mechanisms in the Microlayer using Integrated Total Reflection, Laser Interferometry and Infrared Thermometry Technique." *Heat Transfer Engineering* 36.12 (2015): 1002-1012.
- [40] Graves, R. S., et al. "The thermal conductivity of AISI 304L stainless steel." *International journal of thermophysics* 12.2 (1991): 409-415.
- [41] NASA Jet Propulsion Laboratory Website, <https://masterweb.jpl.nasa.gov/reference/paints.htm>.
- [42] Bergman, Theodore L., et al. *Fundamentals of heat and mass transfer*. John Wiley & Sons, 2011.